Chapter 9

Applications of SMA Bundles in Practical Concrete Structures

Lei Li, Qingbin Li and Fan Zhang

Additional information is available at the end of the chapter

http://dx.doi.org/10.5772/51207

1. Introduction

Shape memory alloy (SMA for short) is a new kind of inter-metallic compound, which can "remember" its original size or shape. Since it was discovered that nickel-titanium showed shape memory effect (SME for short) in 1963, this metal had been being applied in many fields, such as aerospace technology, medical science, automotive industry, et al. At the same time, many constitutive models were developed to simulate its mechanical characteristics, yet there is not a satisfactory result because of its complicated microscopic mechanism.

In the recent twenty years, SMA composites were studied, and the matrix was almost polymer or fiber reinforced resin. During the recent ten years, researches on applying SMA in concrete structures were carried out, but yet limited in laboratory.

In this chapter, the constitutive characteristics of NiTi SMA and its application in practical concrete structures were investigated. Firstly, the transformation characters of the NiTi SMA adopted in this study were obtained through a differential scanning calorimeter (DSC) analysis technology, and then the properties of NiTi SMA during uncompleted transformation process and the effects of plastic deformation on the transformation were studied. The uniaxial tension, SME, and the constrained recovery process of NiTi SMA were examined through an improved 10KN universal material testing machine, effects of the constraint conditions, the maximum tension deformation and the initial phase of SMA on the constrained recovery process were compared and investigated.

To simulate the characteristics of NiTi SMA more effectively, a new constitutive model derived from the internal variable approach was constructed based on the DSC and the uniaxial tension experimental results, a new simple kinetics equation was presented, and the plastic deformation was considered in the constitutive equation.

As the application of SMA in practical concrete structures, a new concept for designing a smart concrete bridge in a freeway was presented against the overload problem in the transport field, and SMA was firstly applied in controlling the deformation of a concrete beam bridge, performances of the concrete beams and the concrete bridge with embedded SMA were examined through a sophisticated test program.

2. One-dimensional constitutive model of sma with an empirical kinetics equation

The characteristics of NiTi SMA were examined through sophisticated testing program, and the constitutive model of NiTi SMA with an empirical kinetics equation was investigated. Firstly, the transformation characters of the NiTi SMA were obtained through a differential scanning calorimetry (DSC) analysis technology, and the properties during incomplete and discontinuous transformation process and the effects of plastic deformation on the transformation were studied. The uniaxial tension, SME and constrained recovery process of NiTi SMA were examined through an improved 10KN universal material testing machine. Experimental results indicated that the phase transformation characters and the mechanical properties could be affected by the loading process considerably, and the plastic deformation should be taken into account. To simulate the characteristics of NiTi SMA more effectively, a one-dimensional constitutive model derived from the internal variable approach with the consideration of the plastic deformation was constructed based on the DSC and the uniaxial tension experimental results, in which a new simple empirical kinetics equation was presented, and the transformation temperature parameters were redefined according to the DSC experimental evidence. Comparison between the numerical and experimental results indicated that this constitutive model could simulate the phase transformation characters, the uniaxial tension, SME and the constrained recovery behavior of NiTi SMA well.

2.1. Background

Since the Shape Memory Effect (SME for short) was observed in Cu-Zn alloy (Greninger & Mooradian, 1938), and in NiTi alloy (Buehler, Gilfrich, & Wiley, 1963), SMA (especially NiTi alloy) has been widely used as intelligent material for its particular characteristics, such as large load capacity, high recovery strain up to 8%, excellent fatigue performance, variable elastic modulus with phase transformation, and especially the two main interesting properties, SME and Pseudo-elasticity (PE) due to the diffusionless martensitic transformation, as discussed elsewhere (Delaey et al., 1974; Krishnan et al., 1974; Warlimont et al., 1974; Funakubo, 1987; Otsuka & Wayman, 1998).

To simulate these specific properties, many constitutive laws have been proposed, such as the phenomenological models (Tanaka & Nagaki, 1982; Tanaka, 1986; Liang, 1990; Brinson, 1993; Zhu et al., 2002), micromechanics models (Sun & Hwang, 1993a, 1993b), 3D model for polycrystalline SMA based on microplane theory (Brocca, Brinson, & Bazant, 2002), etc.

Among them, phenomenological models based on the internal variable method were the most popular used in the practical engineering. The mechanical constitutive equation was derived from the principles of thermodynamics, martensite fraction as an internal variable was used to represent the stage of the transformation, and an empirical kinetics equation was proposed to describe this transformation governed by temperature and stress. The major difference of these models was its specific kinetics equation.

The first phenomenological model was derived by Tanaka and Nagaki (1982) from the first and second laws of thermodynamics and can be written as

$$\sigma = \rho_0 \frac{\partial \Phi}{\partial \varepsilon} = \sigma\left(\varepsilon, T, \xi\right) \tag{1}$$

where σ, ρ_0, Φ, ε, T and ξ represent the second Piola-Kirchhoff stress, the density, Helmholtz free energy, Green strain, temperature and the martensite fraction, respectively.

Equation (1) can be written by differential calculus as

$$\dot{\sigma} = \frac{\partial \sigma}{\partial \varepsilon}\dot{\varepsilon} + \frac{\partial \sigma}{\partial T}\dot{T} + \frac{\partial \sigma}{\partial \xi}\dot{\xi} = D\dot{\varepsilon} + \Theta\dot{T} + \Omega\dot{\xi} \tag{2}$$

where $D = \rho_0 \frac{\partial^2 \Phi}{\partial \varepsilon^2}$ is the modulus of the SMA materials, $\Theta = \rho_0 \frac{\partial^2 \Phi}{\partial \varepsilon \partial T}$ is related to the thermal coefficient of expansion, and $\Omega = \rho_0 \frac{\partial^2 \Phi}{\partial \varepsilon \partial \xi}$ can be regarded as the "transformation tensor".

The relationship between the martensite fraction, the temperature and the stress is expressed by an exponential kinetics equation as

$$\xi_{M \to A} = \exp\left[a_A\left(T - A_s\right) + b_A \sigma\right] \tag{3}$$

for the transformation from martensite to austenite, and

$$\xi_{A \to M} = 1 - \exp\left[a_M\left(T - M_s\right) + b_M \sigma\right] \tag{4}$$

for the transformation from austenite to martensite, where a_A, a_M, b_A, b_M are the material constants related to the transformation temperature, A_s and M_s are the start temperatures of austenite transformation and the martensite transformation, respectively.

Liang (1990) simplified the constitutive model based on Equation (2), material functions were assumed to be constants, and the constitutive relation can be written as

$$\sigma - \sigma_0 = D\left(\varepsilon - \varepsilon_0\right) + \Omega\left(\xi - \xi_0\right) + \Theta\left(T - T_0\right) \tag{5}$$

where the subscript "0" indicates the initial conditions of the materials. Martensite fraction, as a function of stress and temperature during transformation, is represented by an empirically based cosine models as

$$\xi_{M\to A}=\frac{\xi_0}{2}\cos[a_A\left(T-A_s\right)+b_A\sigma]+\frac{\xi_0}{2} \tag{6}$$

for the transformation from martensite to austenite, and

$$\xi_{A\to M}=\frac{1-\xi_0}{2}\cos[a_M\left(T-M_f\right)+b_M\sigma]+\frac{1+\xi_0}{2} \tag{7}$$

for the transformation from austenite to martensite, where ξ_0 is the initial martensite fraction, a_A, a_M, b_A, b_M are the material constants, A_s is the start temperature of austenite transformation, M_f is the finish temperature of martensite transformation.

Brinson (1993) redefined the martensite fraction based on the micromechanics of SMA material as

$$\xi=\xi_S+\xi_T \tag{8}$$

where ξ_s represents the fraction of the stress-induced martensite (or single-crystal martensite) and ξ_T denotes the fraction of the temperature-induced martensite with multiple variants.

Young's modulus was assumed to be non-constant from the experimental evidence as

$$D\left(\varepsilon,\xi,T\right)=D\left(\xi\right)=D_A+\xi\left(D_M-D_A\right) \tag{9}$$

where D_A and D_M are the Young's moduli of austenite and martensite.

The transformation tensor was also redefined as

$$\Omega\left(\xi\right)=\Omega\left(\xi_0\right)+\left(\xi-\xi_0\right)\Omega'\left(\xi_0\right) \tag{10}$$

Because of these improvements, phenomenological models based on the internal variable method could simulate the characteristics of SMA well, such as SME and PE, and have been used in some commercial program for its simple form. Whereas, DSC experiment indicated that there were no apparent transformation start and finish temperatures. And additionally, for the SMA materials used as actuators in practical engineering, not only the stress but also the thermo load determined the transformation process simultaneously, especially the latter. In this section, constitutive model was presented to simulate the characteristics of SMA materials for its practical utilization based on the former effort and the thermal and mechanical experiments. Transformation temperature parameters were redefined, a new simple empirical kinetics equation was presented, and a mechanical equation was developed to describe its mechanical character more directly.

2.2. Experiments and results

2.2.1. Thermodynamics experiment

2.2.1.1. Complete transformation

The Ti-49.5 wt % Ni in this research (binary, straight annealed) was one-way SMA. Its transformation property can be achieved through a DSC apparatus (type: Mettler Toledo DSC821 e), as shown in Fig. 1, the four transformation temperatures can be determined as: martensite transformation start and finish temperatures denoted by M_s and M_f are 33.8 °C and 23.3 °C, austenite transformation start and finish ones (A_s and A_f) are 41.9 °C and 59.6 °C, respectively. It should be noticed that these transformation start and finish temperatures were defined through the DSC diagram artificially, actually the transformation could take place slowly earlier than the transformation start temperature and remain unfinished after the transformation finish temperature, as shown in the experimental curve, thus the recovery forces induced by the transformation might increase or decrease beyond the transformation start and finish temperatures. Accordingly, a new series of parameters were adopted to describe this transformation character more realistically, where T_A and T_M denotes the temperatures corresponding to the peak points of the austenite and martensite transformations, A and M indicate the widths of the transformation peaks, $A \approx \left(A_f - A_s\right)/2e$ and $M \approx \left(M_s - M_f\right)/2e$, and e is the natural constant and equals to 2.71828.

Subtracting the exothermic or the endothermic part of non phase transformation process from the DSC curve (as seen in Fig. 1), normalizing the heat absorbing and releasing capacities, and taking the absolute value, martensite quality fraction ratio versus temperature can be achieved, as shown in Fig. 2.

Calculating the integral of the martensite quality fraction ratio, the relationship of martensite quality fraction versus temperature during the martensite and austenite transformation process can be obtained, as shown in Fig. 3.

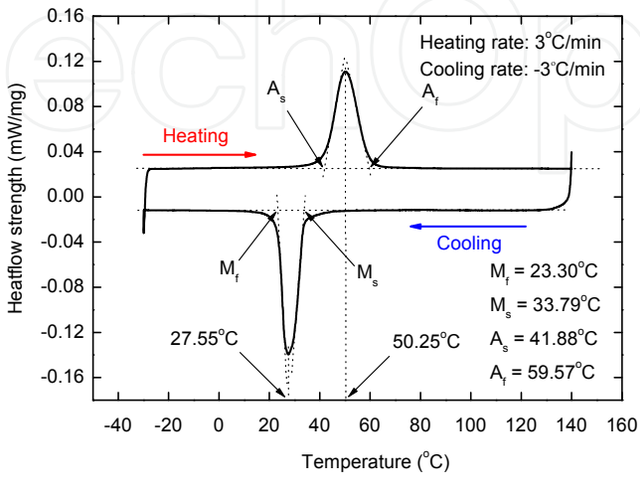

Figure 1. DSC diagram of SMA

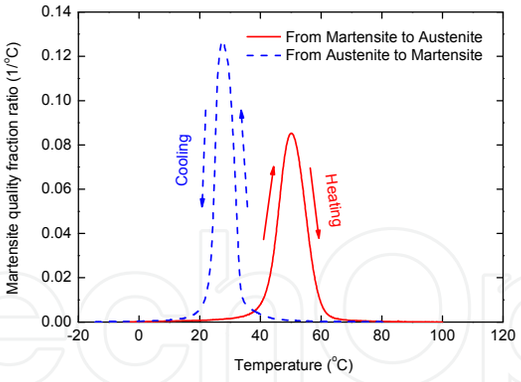

Figure 2. Variation rate of martensite quality fraction versus temperature

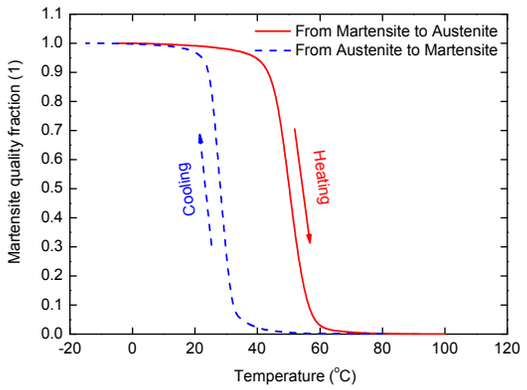

Figure 3. Variation of martensite quality fraction versus temperature

2.2.1.2. Incomplete and discontinuous transformation

If the initial state is not the complete martensite or austenite, the phase transformation will be different.

At the temperature of 140 °C, the initial state of SMA is pure austenite, cooling will induce the transformation from austenite to martensite, while at half of this transformation, heating will lead to the reverse transformation from the new generated martensite to austenite, the start and finish temperature and the shape of the peak are similar to the ones of the complete austenite transformation, but the peak value is smaller than the complete transformation one, as shown in Fig. 4.

Similarly, at the temperature of -30 °C, the initial state is pure martensite, heating will induce the transformation from martensite to austenite, while at half of the transformation, cooling will lead to the transformation from the new generated austenite to martensite, the start and finish temperatures and the shape of the peak are similar to those of the complete martensite transformation, but the peak value becomes smaller than the complete transformation one, as shown in Fig. 5.

These phenomena indicate that the martensite transformation intensity is related to the initial austenite quality fraction and the austenite transformation intensity is related to the initial martensite quality fraction. Accordingly, it is assumed that the martensite

transformation intensity is proportional to the initial austenite fraction, and the austenite transformation intensity is proportional to the initial martensite fraction.

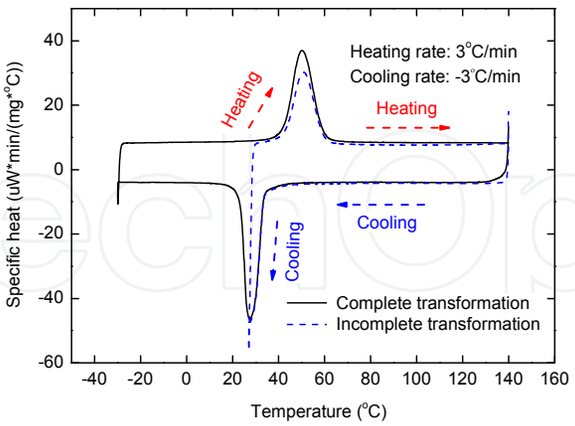

Figure 4. Incomplete transformation from martensite to austenite

During the transformation from austenite to martensite, i.e., the cooling process, if the small heating does not induce the transformation from martensite to austenite, the martensite transformation will continue during the subsequent cooling process, as shown in Fig. 6.

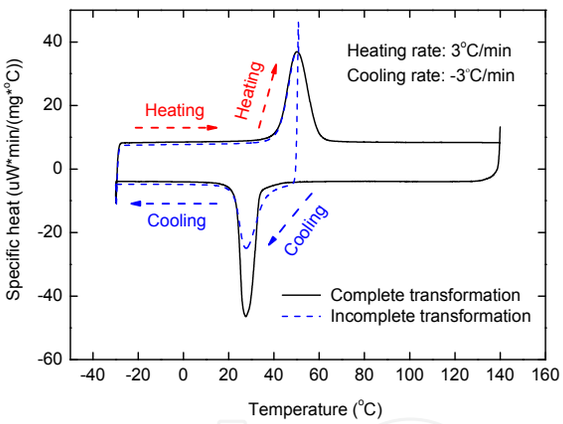

Figure 5. Incomplete transformation from austenite to martensite

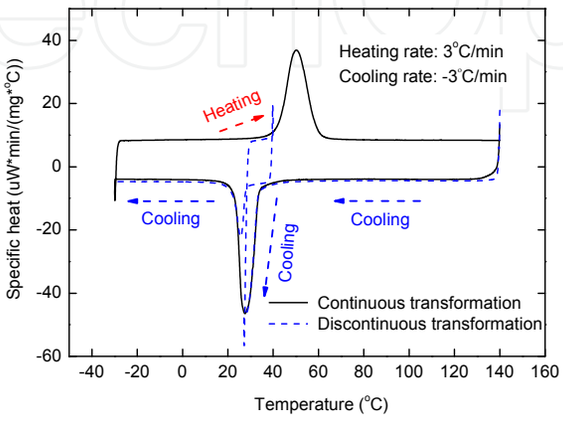

Figure 6. Discontinuous transformation from austenite to martensite

Similarly, during the transformation from martensite to austenite, i.e., the heating process, if the small cooling does not induce the transformation from austenite to martensite, the austenite transformation will continue during the subsequent heating process, as shown in Fig. 7.

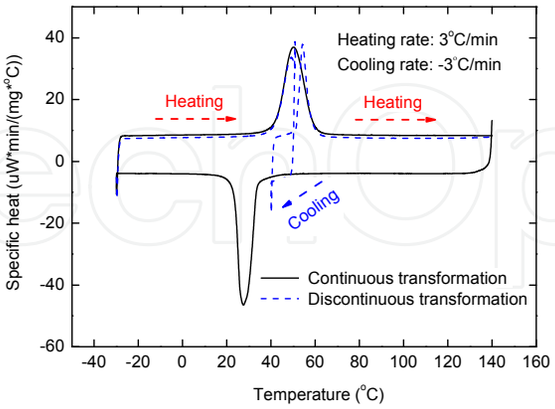

Figure 7. Discontinuous transformation from martensite to austenite

2.2.1.3. Influence of plastic deformation

Plastic deformation can also change the transformation properties of SMA materials. Stretch SMA to its strain limit, great plastic deformation will be induced, and the DSC experimental result can be achieved as shown in Fig. 8. The temperatures of the austenite transformation and martensite transformations become higher, the width of the peak become wider, and the peak value become smaller than these before tension. This phenomenon comes from the variation of the crystal structure and the internal stress induced by the plastic deformation. Actually, the transformation properties of the SMA crystal cell did not change, just the micro structure of SMA material varied.

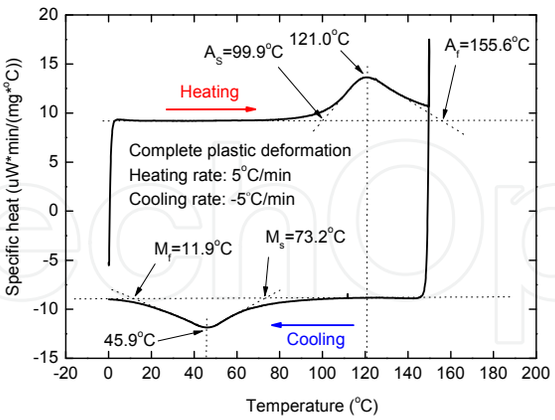

Figure 8. DSC analysis of plastic deformed SMA

2.2.2. Mechanics experiment

Mechanical experiment was carried out to determine the material characteristics and parameters through a WDW-10 universal material test machine. The experimental equipment is shown in Fig. 9. Pt100 platinum electric resistance temperature sensors were

plastered on the SMA wire with silica gel to monitor its temperature, strain gauge was used to measure its strain. Load applied on the SMA wire, environment temperature, current intensity, and the voltage of SMA wire between the two points of the strain gauge were also monitored at the same time. All these signals were acquired through a 16-channel dynamic data acquisition system.

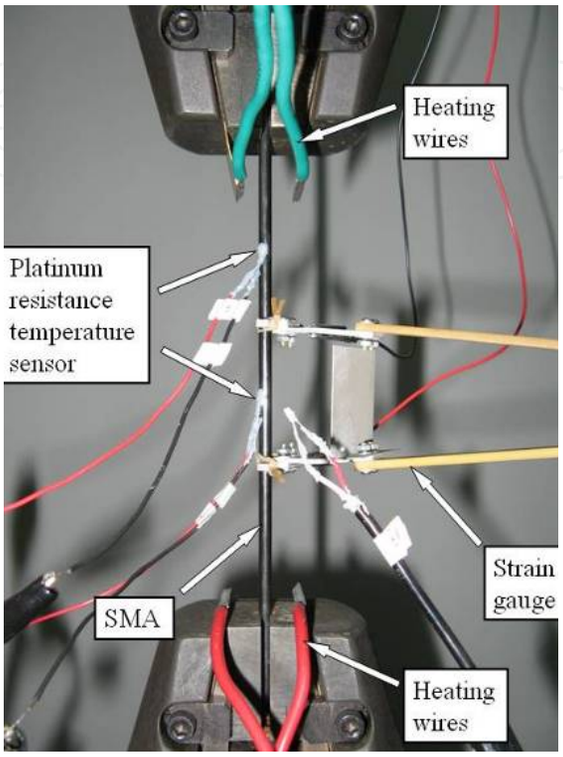

Figure 9. Uniaxial tension test equipment

2.2.2.1. Uniaxial tension test

The first test was made with constant ambient temperature. SMA wire samples were heated by boiled water firstly, and then cooled by ice water, thus the initial state of the samples was pure twinned martensite. Experimental results are shown in Fig. 10. There are two horizontal "plastic" stages during the tension process of 1mm diameter SMA wire. The first stage was derived from the detwinning process of the twinned martensite, i.e. from twinned martensite to single martensite, which can be named "pseudo-plasticity" that could be recovered by heating, and the second stage was induced by plastic deformation, which was the "real plasticity".

The second uniaxial tension test was carried out with different SMA temperatures. Similarly, SMA wire samples were also pretreated to obtain different initial state. For example, if the sample was heated by boiled water, then cooled by ice water, and then heated to the test temperature of 44.5 °C by electric current, the initial state will be twinned martensite. However, if the sample was heated by boiled water, and then cooled to the test temperature of 44.5 °C, the initial state will be austenite. During the experimental process, testing temperatures were kept constant by adjusting the current intensity.

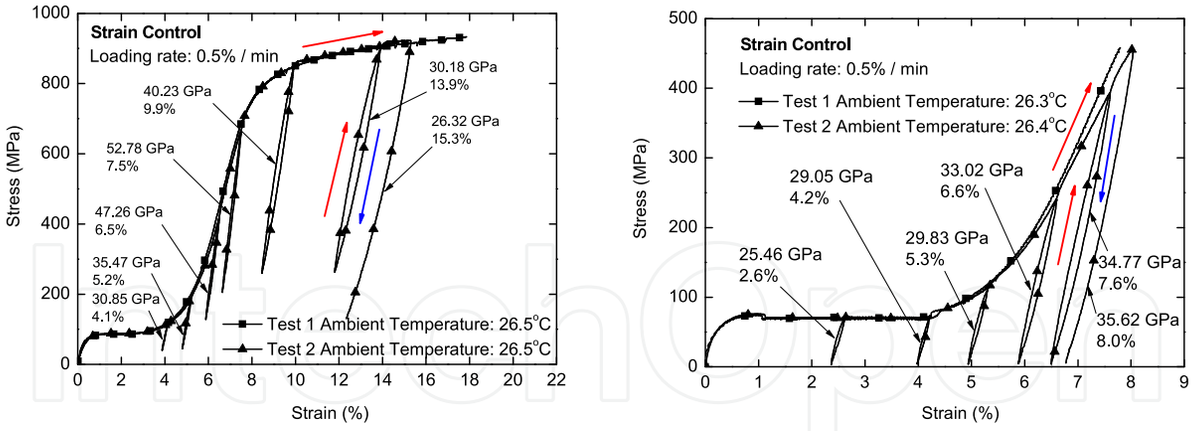

(a). SMA diameter: 1mm (b). SMA diameter: 5mm

Figure 10. Uniaxial tension test

Elastic moduli of austenite, twinned martensite and detwinned martensite can be determined as 85.5 GPa, 28.24 GPa and 25.75 GPa, respectively based on the experimental result, as shown in Fig. 11, where "M" means the initial state of the sample as twinned martensite, and "A" as austenite. At different ambient temperatures, the initial elastic moduli of austenite are the same. In the ambient temperature of 44.5 °C, no matter what the initial state is, the critical stress that leads to the stress-induced martensite transformation or the detwinning process of twinned martensite was almost equal.

During the heating recovery process under stress free conditions, the critical temperatures of the thermo-induced austenite transformation were almost the same. Otherwise, the unrecoverable stain of the specimen stretched from martensite initial state was a little bit bigger than that from austenite, as shown in Fig. 12.

For the sample starting from complete austenite, the critical stress inducing martensite transformation increased with the temperature. The statistic result is shown in Fig. 13.

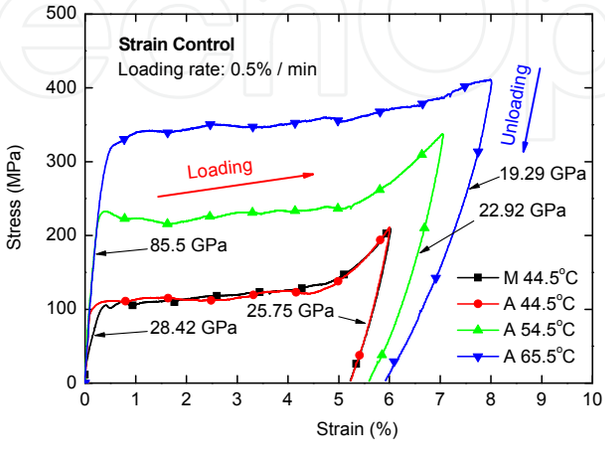

Figure 11. Uniaxial tension processes under different ambient temperatures

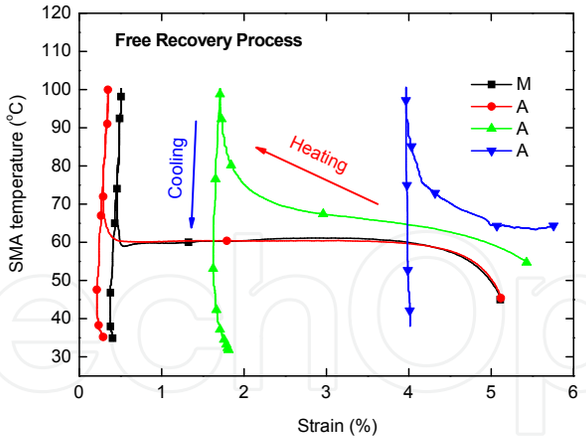

Figure 12. Free recovery processes of SMA after loading with different temperatures

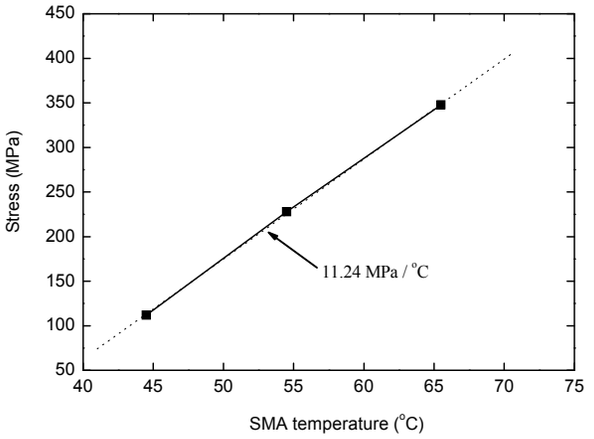

Figure 13. Variation of critical stress with stress induced martensite transformation temperature

2.2.2.2. SME test

SMA samples with 5mm in diameter were firstly stretched to 4.2%, 5.3%, 6.6%, 7.6%, respectively, and then heated in strain free conditions, this loading cycle was repeated for three times.

For the sample with the loading strain of 5.3%, variation of stress with strain during the uniaxial tension process is shown in Fig. 14, and the variation of strain with temperature during the free heating process is shown in Fig. 15. Stress-strain curve of SMA with other maximum loading strains are similar to Fig 14 and Fig. 15.

Experimental results indicated that the plastic deformation increased with the loading times, and during the free recovery process, critical temperature inducing the reverse martensite transformation decreased with loading times, and the recoverable strain became smaller and smaller.

Comparing the samples with different maximum tension strain, variations of stress with strain and that of strain with temperature during the second loading times and free recovery process are shown in Fig.s 16 and 17, respectively. Test results during the first and the third loading cycles are similar to each other.

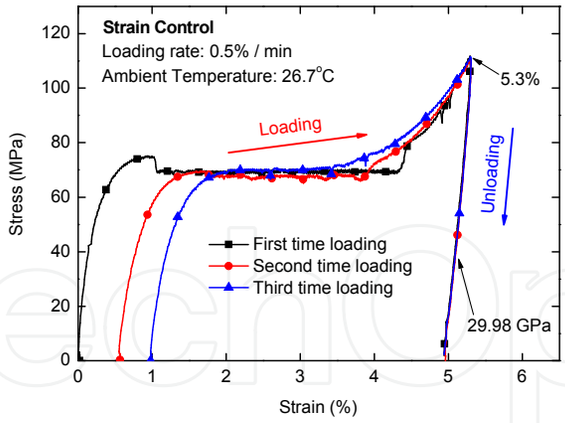

Figure 14. Stress-strain curve of SMA in different loading times

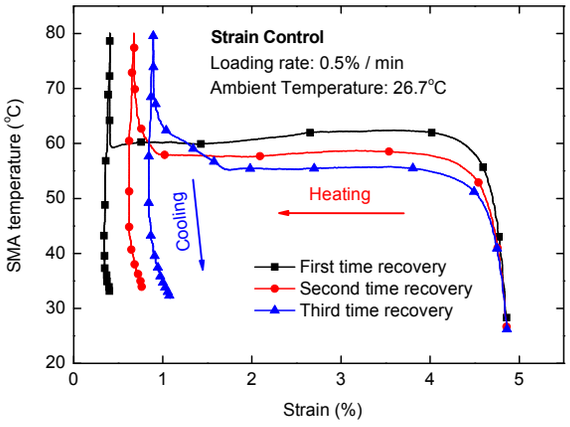

Figure 15. Temperature-strain curve of SMA in different loading times

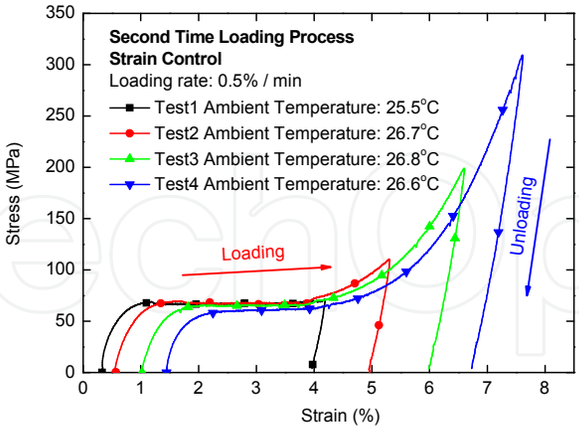

Figure 16. Stress-strain curve of SMA in different maximum loading deformations

Additionally, statistical results indicated that the critical temperature inducing the reverse martensite transformation increased with the maximum deformation, decreased with the loading/unloading times, as shown in Fig. 18. At the same time, the plastic deformation increased with the maximum deformation and the loading/unloading times, as shown in Fig. 19.

According to the experimental curve, the plastic deformation increased with the initial tension strain during the loading and unloading process, and the critical temperature inducing the austenite transformation increased with the initial tension strain, also increased with the plastic deformation.

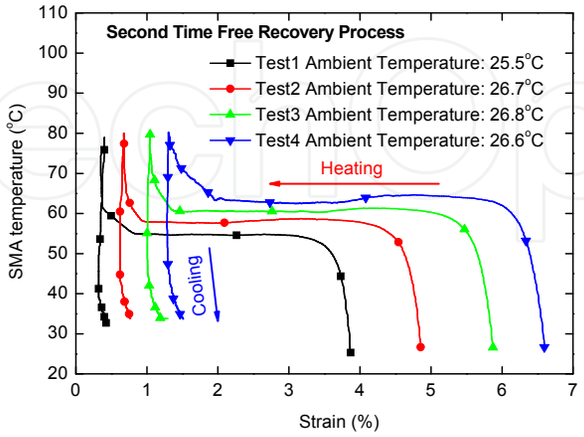

Figure 17. Temperature-strain curve of SMA in different maximum loading deformations

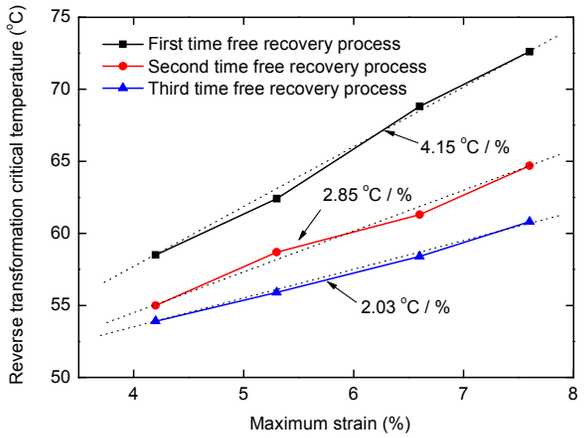

Figure 18. Variation property of transformation critical temperature with maximum loading strain

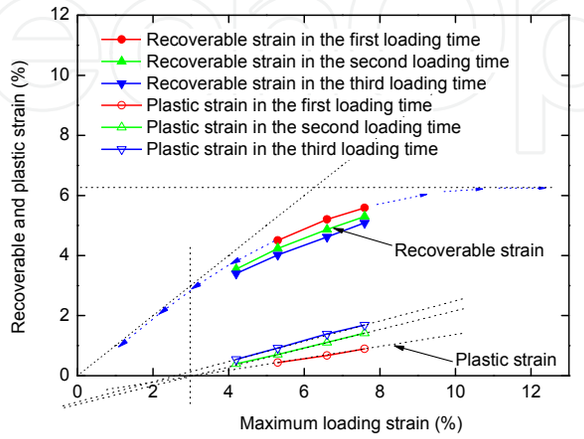

Figure 19. Variation property of recoverable and plastic strain with maximum loading strain

2.2.2.3. Recovery test under constrained condition

The recovery test under constrained condition contained five loading paths: (1) strain-control loading to 4.2% under normal temperature; (2) heating to 90 °C and then cooling to 30 °C under elastic constrained condition in the first time; (3) heating to 90 °C and then cooling to 30 °C under elastic constrained condition in the second, third and fourth times; (4) unloading to free condition; (5) heating to 100 °C and then cooling to 30 °C under free condition.

In the initial state of twinned martensite, the elastic constrained recovery test of SMA is shown in Fig. 20. Test results under different constrained conditions, initial state and maximum strain are similar in form.

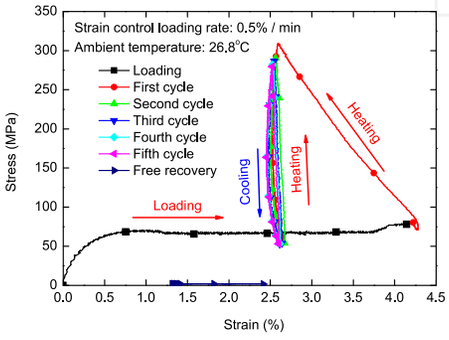

(a). Stress-strain curve

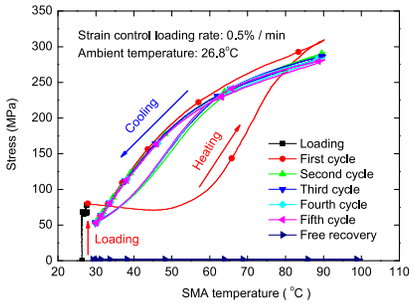

(b). Stress-temperature curve

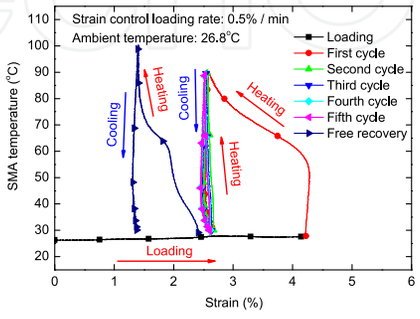

(c). Temperature-strain curve

Figure 20. Constrained recovery test

Because constraint elastic modulus during the first heating process was smaller than that of the subsequent second to fifth heating/cooling process, relationships between stress and strain, stress and temperature, and temperature and strain, were different correspondingly. In the first heating process, the stress increased gradually, the strain decreased and some deformation of SMA restored. In the following heating and cooling process, the strain almost remained, the stress increased with temperature rising and decreased with temperature dropping, forming a hysteretic circle, and the variation rate of stress with temperature changed in the range of 2.4 MPa ~ 8 MPa / °C. During the heating process under stress free state, the strain recovery course of SMA with temperature showed two obvious stages, as shown in Fig. 20 (c).

2.3. Constitutive model

2.3.1. Physical equation

According to the macro-phenomenon, deformation of SMA during thermo and stress loading process can be divided into four components: (1) macro recoverable deformation caused by martensite transformation, mainly determined by single crystal martensite percentage; (2) elastic deformation; (3) Thermal expansion deformation; (4) Plastic deformation. Thus, the macro physical equation of SMA in strain form during the temperature and stress loading process can be expressed as

$$\begin{aligned}\varepsilon &= \varepsilon^R + \varepsilon^E + \varepsilon^T + \varepsilon^P \\ &= \varepsilon_{res} \bullet \xi_{SM} + \frac{\sigma}{\left(\xi_{SM} \bullet E_{SM} + \xi_{TM} \bullet E_{TM} + \xi_A \bullet E_A\right)} + \left(\xi_{SM} \bullet \eta_{SM} + \xi_{TM} \bullet \eta_{TM} + \xi_A \bullet \eta_A\right) \bullet \left(T - T_0\right) + \varepsilon^P\end{aligned} \quad (11)$$

where ε is the dimensionless macro total strain, positive for stretch; ε^R, ε^E, ε^T, ε^P denote the dimensionless recoverable transformation, elastic, thermal expansion and plastic strains, respectively; ε_{res} is the maximum recoverable strain; σ is the macro stress, positive for stretch (unit: MPa). E_{SM}, E_{TM}, E_A denote the elastic moduli of single crystal martensite, twinned martensite and austenite, respectively (units: GPa). η_{SM}, η_{TM}, η_A denote the thermal expansion coefficients of single crystal martensite, twinned martensite and austenite, respectively (units: $1/^{\circ}\mathrm{C}$). ξ_{SM}, ξ_{TM}, ξ_A denote the quality fractions of single crystal martensite, twinned martensite and the austenite, respectively, with $\xi_{SM} + \xi_{TM} + \xi_A$ equals to 1. T is the temperature of SMA (unit: °C). T_0 is the initial temperature of SMA (unit: °C).

2.3.2. Kinetics equation

DSC experiments showed that, there were no obvious transformation start and finish temperatures during the transformation process. In this section, the single transformation characteristic temperatures, as well as the parameters that reflect the width of the endothermic and exothermic peaks, are adopted to simulate the phase transformation of SMA, and the corresponding kinetics equation is established at the same time.

During the transformation process, there are three crystal structures in SMA material, twinned martensite, single martensite, and austenite, respectively, thus there are six phase transformation processes theoretically. In this section, each phase transition process is analyzed based on the DSC experiments, and the corresponding transformation principles and conditions are presented.

2.3.2.1. Transformation from twinned martensite to austenite

Transformation condition: Assuming in one-dimensional terms, only heating can lead to this phase transition from twinned martensite to austenite.

Transformation principle: For the transformation from twinned martensite to austenite, if the reverse transformation from austenite to twinned martensite did not occur during the process, a small cooling will not affect its subsequent transformation process, as shown in Fig. 7.

However, if the reverse transformation process happened and induced a lot of austenitic to twinned martensite, then the extent of the following transformation from twinned martensite to austenite required reduction in accordance with the quality fraction of the current twinned martensite, as shown in Fig. 4.

Thus, the kinetics equation from twinned martensite to austenite can be acquired as

$$\xi_{TM} = \frac{\xi_{TM0}}{1 + e^{\frac{T - T_A}{A}}} \tag{12}$$

where ξ_{TM0} is the initial quality fraction of twinned martensite; T_A is the characteristic temperature for austenite transformation, and numerically equivalent to the temperature where the complete austenite transformation goes into the half, and is equivalent to the peak temperature of the DSC endothermic curve approximately; A is the transformation parameter reflecting the width of the endothermic peak, and numerically equivalent to $\frac{A_f - A_s}{2e}$, here A_s, A_f denote the start and finish temperatures of austenite transformation defined by the traditional method. e is the natural constant and equals to 2.71828.

2.3.2.2. Transformation from austenite to twinned martensite

Transformation condition: Assuming in one-dimensional terms, only cooling can lead to this phase transition from austenite to twinned martensite.

Transformation principle: For the transformation from austenite to twinned martensite, if the reverse transformation from twinned martensite to austenite did not occur during the process, a small heating will not affect its subsequent transformation process, as shown in Fig. 6.

However, if the reverse transformation process happened and induced a lot of twinned martensite to austenitic, the extent of the following transformation from austenite to twinned martensite required reduction in accordance with the quality fraction of the current austenite, as shown in Fig. 5.

Thus, the kinetics equation from austenite to twinned martensite can be acquired as

$$\xi_{TM} = \frac{\left(1-\xi_{TM0}\right)}{1+e^{\frac{T-T_M}{M}}} + \xi_{TM0} \tag{13}$$

where T_M is the characteristic temperature for martensite transformation, and numerically equals to the temperature where the complete martensite transformation goes into the half, and is equivalent to the peak temperature of the DSC exothermic curve approximately; M is the transformation parameter reflecting the width of the exothermic peak, and numerically equivalent to $\frac{M_s - M_f}{2e}$, here M_s, M_f denote the start and finish temperatures of martensite transformation defined by the traditional method.

2.3.2.3. Transformation from twinned martensite to single martensite

Transformation condition: Assuming in one-dimensional terms, only the increase of stress can lead to this phase transition from twinned martensite to single martensite.

Transformation principle: During the uniaxial tension process, for the transformation from twinned martensite to single martensite, if the none macro press stress occur during unloading process, this unloading will not affect the transformation of the subsequent reloading process.

During the phase transition process, taking the twinned martensite as austenitic, this transformation will be similar to the transformation from austenite to single martensite, only with the different phase transition peak temperature, and the transformation parameters and impact coefficient of the stress on the temperature still adopted the values of transformation from austenite to twinned martensite.

Therefore, based on the kinetics of the transformation from austenite to twinned martensite, kinetics of the transformation from twinned martensite to single one can be achieved as

$$\xi_{SM} = \frac{1}{1+e^{\frac{T-\frac{\sigma^i}{C_{M'}}-T_{M'}}{M'}}} \tag{14}$$

or

$$\xi_{TM} = \frac{1}{1+e^{\frac{\sigma^i-\sigma^i_{crit}}{C_{M'}\bullet M'}}} \tag{15}$$

where σ^i denotes the average internal stress between the crystals (unit: MPa); $T_{M'}$ is the transformation characteristic temperature; M' is the transformation parameter; $C_{M'}$ denotes the impact coefficient of stress on transformation temperature; σ^i_{crit} denotes the

average internal stress between the crystals where the full de-twinned process occurred on the half (unit: MPa).

2.3.2.4. Transformation from single martensite to twinned one

Transformation condition: For uniaxial tension process, macro-stress and the temperature will not induce the transformation from single martensite to twinned one. However, under repeated stretch-press loading, the martensites with different directions will change its direction repeatedly, and this process corresponds to the SMA rubber-like plastic phenomenon.

2.3.2.5. Transformation from single martensite to austenite

Transformation condition: Assuming in one-dimensional terms, heating and the decrease of stress can lead to this phase transition from single martensite to austenite.

Transformation principle: As similar to the transformation from twinned martensite to austenite, for the transformation from single martensite to austenite, if the reverse transformation from austenite to single martensite did not occur during the process, a small cooling or increase of stress will not affect its subsequent transformation process.

However, if the reverse transformation process happened and induced a lot of austenitic to single martensite, then the extent of the following transformation from single martensite to austenite required reduction in accordance with the quality percentage of the current single martensite.

Thus, the kinetics equation from single martensite to austenite can be acquired as

$$\xi_{SM} = \frac{\xi_{SM0}}{1 + e^{\frac{T - \frac{\sigma^i}{C_A} - T_A}{A}}} \tag{16}$$

where ξ_{SM0} is the initial quality fraction of single martensite.

2.3.2.6. Transformation from austenite to single martensite

Transformation condition: Assuming in one-dimensional terms, cooling and increase of stress can lead to this phase transition from austenite to single martensite.

Transformation principle: As similar to the transformation from austenite to twinned martensite, for the transformation from austenite to single martensite, if the reverse transformation from single martensite to austenite did not occur during the process, a small heating or decrease of stress will not affect its subsequent transformation process.

However, if the reverse transformation process happened and induced a lot of single martensite to austenitic, then the extent of the following transformation from austenite to single martensite required reduction in accordance with the quality percentage of the current austenite.

Thus, the kinetics equation from austenite to single martensite can be acquired as

$$\xi_{SM} = \frac{\left(1-\xi_{SM0}\right)}{1+e^{\frac{T-\frac{\sigma^i}{C_M}-T_M}{M}}} + \xi_{SM0} \tag{17}$$

2.3.2.7. Parameter variation properties of the kinetics

At the same time, DSC experiments showed that, even for the same material components and the same diameter of the SMA, the transformation of the material would be very different after experiencing loading and plastic deformation, as shown in Fig. 8, and these changes must be considered in the constitutive model.

For the SMA of 1mm in diameter, in austenite transformation process, after undergoing the plastic deformation, the transformation peak temperature changes from 50.25 °C to 121.0 °C, and the transformation parameter changes from 3.25 to 10.25. Similarly, in the martensite transformation process, the transformation peak temperature changes from 27.55 oC to 45.9 °C, and the transformation parameter changes from 1.93 to 11.28.

It must be pointed out that these variations are apt for the SMA with 1 mm in diameter. For the SMA with 5 mm in diameter, the change scope of these parameters will be different and can be determined by experiment.

2.3.3. Consideration of the plastic deformation

In the first loading process, after stretching to different deformations and heating under free condition, plastic deformations for different initial deformations are shown in Fig. 19.

Experimental results indicated that, when the maximum tensile strain exceeded 3%, the plastic deformation increment would be linearly related to the maximum tensile strain increment, thus, the experience equation of the plastic evolution could be achieved as follows

$$\varepsilon^P = 0.198 \times \left(\varepsilon - 0.03\right) \text{ and } \varepsilon^P \geq 0 \tag{18}$$

It must be pointed out that, this equation is the fitted results of the uniaxial tensile test at room temperature. For another SMA material under different temperature, variation of the plastic deformation with the strain will be very different. Additionally, this equation is only applicable to simulate plastic evolution characteristics during the first loading process, but not the second and the third loading processes.

2.4. Numerical simulation and comparison with the experimental results

Two parts are included in this section, one is the determination of the parameters in the kinetics equation based on the DSC test results and the calculation of the phase transformation, uniaxial tension, SME and the constrained recovery curves, the other is the comparison with the experimental results.

2.4.1. Determination of the parameters in constitutive equation

The transformation characteristics was calculated through the kinetics equation directly and compared with the experimental results. The SMA uniaxial tension, SME and the constrained recovery stress-strain-temperature curves were calculated through the incremental form of the constitutive model. The Parameters used in the calculating process were determined through the following principles:

1. Transformation characteristic temperature and parameters of the kinetics were determined through the DSC test results;
2. The macro physical parameters, such as the elastic modulus, thermal expansion coefficient adopted the experimental result;
3. Because the characteristics temperature and transformation parameters change with the loading process, therefore, in the calculating program, these parameters were adjusted according to the test results of SMA with 1 mm in diameter;
4. The critical value of the internal stress was adjusted based on the experimental critical stress in uniaxial tension.

2.4.2. Verification of SMA transformation property

According to the variation curve of martensite quality percentage with the temperature of martensite transformation and reverse one (Fig. 3), the parameters of the kinetics equation can be achieved through the numerical fitting of the test results, as shown in Table 1.

	Transformation characteristics temperature (°C)	Transformation parameter (°C)
Martensite transformation process	28.2	1.947
Reverse martensite transformation process	50.14	2.999

Table 1. Transformation parameters determined by DSC test

Using the parameters calibrated by the numerical fitting, variation curve of martensite quality percentage with temperature can be calculated. The results with comparison of the test ones are shown in Fig. 21. Additionally, variation curve of martensite quality percentage changing rate with temperature can be calculated as shown in Fig. 22, with comparison of the test ones.

These comparisons between the numerical and the experimental results indicate that the kinetics equation proposed can simulate the transformation properties of SMA more practically, there are not obvious start and finish temperatures in the calculated curve during the transformation process, the calculated exothermic and endothermic peaks are consistent well with the experimental ones.

2.4.3. Comparison of the uniaxial tension, SME and controlled recovery curve

Through the constitutive model with differential form, the uniaxial tension, SME and controlled recovery curve of SMA with 5 mm in diameter can be calculated by program, and compared with the test results, as shown in Fig.s 23-25.

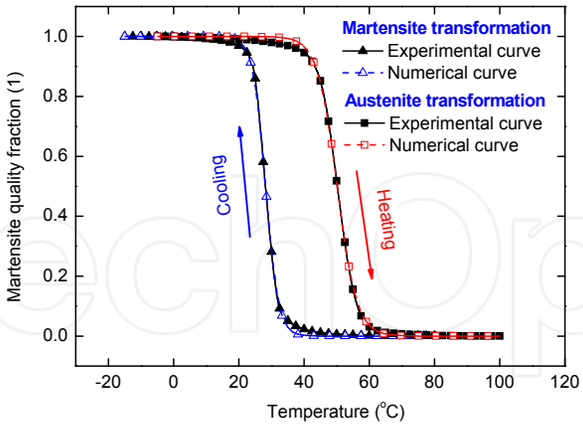

Figure 21. Comparison between experimental and calculated curve of martensite quality fraction versus temperature

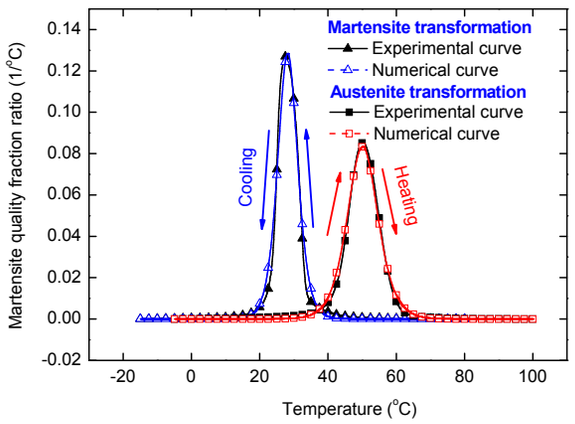

Figure 22. Comparison between experimental and calculated curve of martensite quality fraction ratio versus temperature

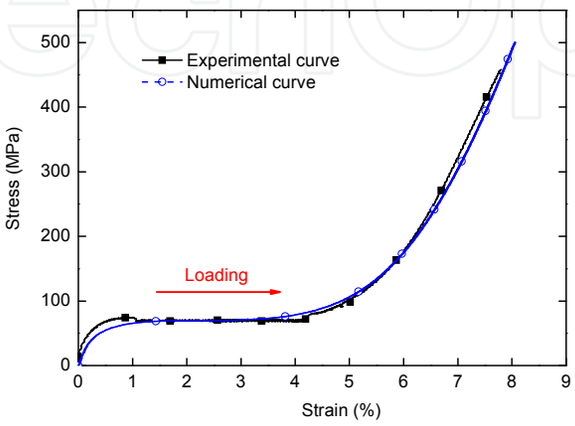

Figure 23. Comparison between experimental and calculated curve of uniaxial tension process

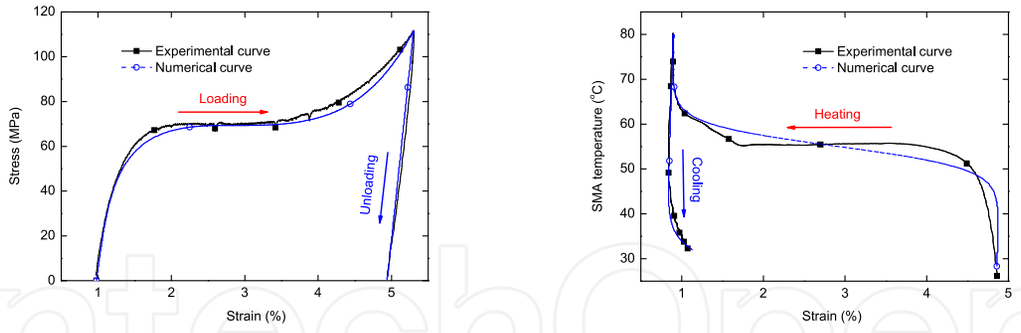

(a). Stress-strain curve (b). Temperature-strain curve

Figure 24. Comparison between experimental and calculated curve of the third times SME process

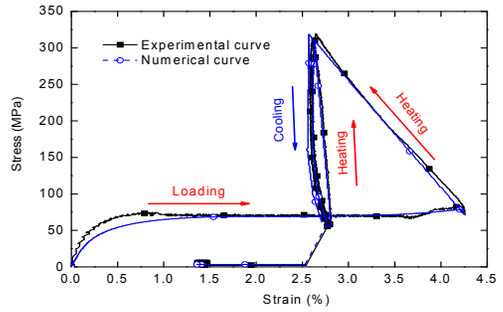

(a). Stress-strain curve

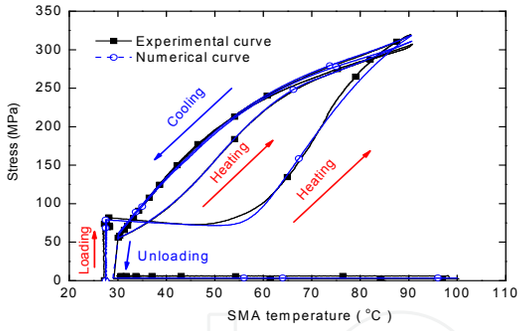

(b). Stress-temperature curve

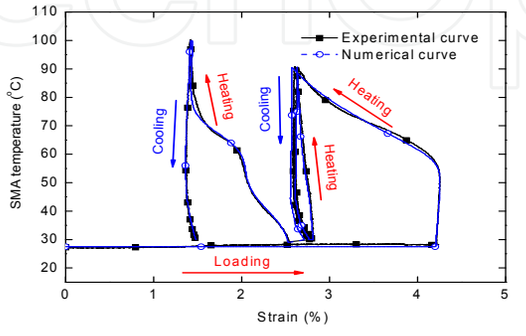

(c). Temperature-strain curve

Figure 25. Comparison between experimental and calculated curve of constrained recovery process

Numerical results indicate that, based on the well forecast for the phase transformation properties, the constitutive model can simulate the uniaxial tension, SME and controlled recovery process of SMA more accurately.

2.5. Conclusions

A constitutive model in strain form with a new simple empirical kinetics equation is presented based on the DSC and uniaxial tension test, and the plastic deformation is considered. Transformation temperature parameters that denote the peak temperature and peak width of the endothermic and exothermic process were adopted to simulate the transformation characteristics of SMA more practically. Transformation conditions and properties of the six transformation processes were analyzed.

At the same time, physical and kinetics parameters were identified through the DSC and the uniaxial test analysis for SMA, programs were adopted for calculating the phase transformation and uniaxial tension process. Comparison between the simulating and experimental results shows that the established constitutive model can simulate the martensite and the reverse transformation, as well as the uniaxial tension, SME and constraint recovery process, more accurately.

3. Behavior of smart concrete beams with embedded SMA bundles

The behavior of smart concrete beams with embedded SMA bundles was investigated. Two beams measuring 1996cm×99cm×85cm, which will be integrated into a smart bridge in a freeway, were manufactured and examined. Each beam contained six trusses of SMA bundles used as actuators to achieve recovery force. The SMA bundles were connected with pre-stressing steel strands and separated from the concrete matrix, so that the temperature interchange between SMA bundles and the matrix could be decreased as small as possible. Some temperature sensors, reinforcement meters and displacement sensors were used to monitor the active control effect of SMA bundles, all the data were acquired through a 16-channel dynamic data-acquisition system, and each beam was examined several times with different activating current intensity. Experimental results indicated that the recovery force induced by SMA bundles was significant and controllable, the deflection generated by the SMA bundles at the middle span of the beam was about 0.44mm, and the capability of resisting overload of each beam was about 2.98 KN (average). A relationship between SMA temperature and activating / inactivating time was also formulated. The conclusion is that SMA could be used in civil engineering structures either from technological or economic aspect.

3.1. Background

With the developments of materials science, engineering technology, data acquisition and computer technology, 'Intelligent' materials, such as Electrorheological fluid, piezoelectric ceramic, shape memory alloys, etc, have opened the door for many useful applications, e.g.

civil engineering, automotive industry, aerospace technology, medical science (Crawley, 1994; Matsuzaki, 1997; Srinivasan & Mcfarland, 2001). Implementation of smart structures has become feasible, and much effort has been made in these fields.

3.1.1. SMA smart structure

Because of the merits of SMA, many researchers have been trying their efforts to apply it in smart structures. These applications were mainly based on the two properties of SMA: one is the shape change with temperature, where SMA fibers are pre-strained during the curing process and prevented from a transformation to austenite, if the temperature rises during the operational cycle, the fibers transform into austenite and tend to contract, and the recovery tensile stresses develop due to the constraint of the matrix; The other is the mechanical characters variation, where unstrained SMA fibers are embedded within the composite, increase or decrease of the temperature alters the elastic modulus or the damping property of SMA, consequently changing the property of the composite. Due to these properties, SMA is usually used to generate bending (Chaudhry & Rogers, 1991; Lagoudas & Tadjbakhsh, 1992), control bucking and postbucking (Baz & Tampa, 1989; Choi et al., 1999, 2000), induce or depress vibration (Baz, Imam, & Mccoy, 1990; Anders, Rogers & Fuller, 1990; Baz, Poh, & Gilheany, 1995; Lau, Zhou, & Tao, 2002), isolate seism (Graesser & Cozzarelli, 1991).

Jonnalagadda, Kline, & Sottos (1997) investigated the interaction between SMA wires and a host polymer matrix by correlating local displacements and stress fields induced by the embedded wires with SMA/polymer adhesion, interfacial bond strength was measured for four different SMA surface treatments: untreated, acid etched, hand sanded and sandblasted. Song, Kelly, & Agrawal (2000) presented the design and experimental results of the active position control of a SMA wire actuated composite beam, which has a honeycomb structure with SMA wire embedded in one of its face sheets, a robust controller was designed and implemented to actively control the tip position of the composite beam.

3.1.2. SMA-based concrete structures

In the recent ten years, many researches have been done for the application of these intelligent materials in civil engineering. Maji & Negret (1998) carried out their laboratory studies on concrete (mortar) beams (30.5cm×2.5cm×1.3cm), where SME in NiTi was utilized as a way of inducing additional pre-stressing in concrete. Strands made with NiTi SMA ($4\Phi 0.64mm$) were elongated beyond their plastic limit and subsequently embedded in concrete beams, upon electrical heating, the SMA strands shrunk and induced deflection and failure in concrete. In this study, the temperature rise of the beam was formulated based on heat transfer theory, assuming that the temperature of SMA was the average temperature of the beam.

Deng et al. (2003) studied the behavior of concrete specimens uniaxially embedded with shape memory alloy wires actuated by electrical current. Two kinds of specimens with

different number of SMA wires were studied, the diameter of the SMA employed in the matrix was 3.5mm and the pre-strains were 8% and 6%. Many factors affecting the behavior of concrete specimens were examined through experiments, such as actuating electrical current mode, initial pre-strain of SMA, actuation times, and initial ambient temperature. The experimental results indicated that the axial strain could be adjusted easily by changing the value of electrical current intensity or the actuating time of the SMA actuator.

However, the application of smart concrete beams with embedded shape memory alloy bundles has not been reported to date. The above researches were mostly carried out in laboratory, but a potential practical use of smart concrete beams needs an adequate study on them, because the characteristics of small specimens, as well as the manufacture process, may be very different with those of the engineering structures, thus it is necessary to make a practical engineering investigation in civil structures. Accordingly, two concrete beams measuring 1996cm×99cm×85cm were manufactured and investigated in this section.

3.2. Experimental program

3.2.1. Materials

The materials used for the host concrete were type I Portland cement, crushed limestone, and river sand. A high-rang water reducer was used to achieve good workability. The mix proportion by weight was cement: sand: aggregate: water: admixture = 1: 1.187: 2.412: 0.329: 0.008. The compressive strength of the concrete (cubic specimen) for 28 days was 53.47 MPa.

The seven-wire high-strength steel strands with the diameter of 15.24mm were used to apply conventional pre-stressing force in this experiment, its tensile strength is 1860 MPa, the working stress was controlled to 1395 MPa, and the modulus is 180 GPa. As ordinary reinforced concrete beam, steel reinforcement was used to construct the reinforcing cage.

The Ti-49.5 wt % Ni for our research (binary, straight annealed) was one-way SMA. Its transformation temperatures were determined as 25.3 °C (Mf), 36.3 °C (Ms), 44.8 °C (As) and 66.4 °C (Af) through a DSC (differential scanning calorimetry) analysis (Fig. 26).

The specific stress-strain behavior of this SMA bar under different temperatures and constrained condition were, as shown in Fig. 27, achieved through a sophisticated test method with a 10KN universal material testing machine.

The maximum recovery strain was larger than 5%, and the tensile strength was about 940 MPa (corresponding to the ambient temperature: 22.3 °C) with the ultimate strain of 19.1% (Fig. 27a). When the SMA is free to deform at a relative lower temperature, large plastic strain (about 4%) is induced, but upon heating, this plastic strain disappears, with only a small unrecovery strain (smaller than 0.2%) in the end (Fig. 27b). Whereas, if the SMA recovery is constrained, large stresses should be induced (Fig. 27c), this behavior is the principle of SMA used as actuators.

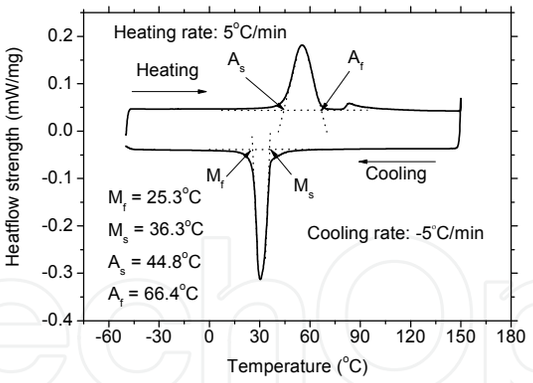

Figure 26. DSC thermogram for NiTi SMA

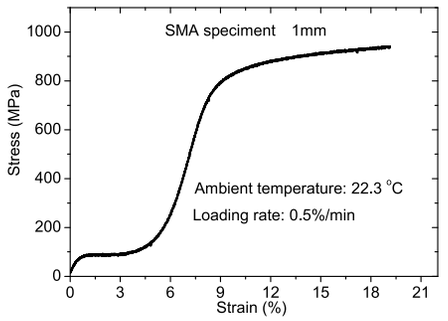

(a). Complete uniaxial tension stress-strain curve of SMA

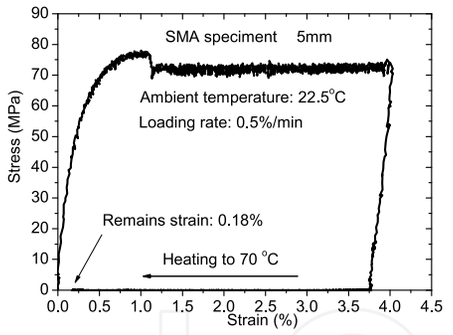

(b). SME of SMA

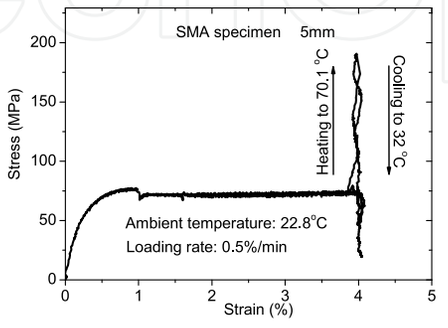

(c). Constrained curve of SMA

Figure 27. Stress-strain behavior of NiTi SMA

As depicted in Fig. 28, a seven-wire SMA bundle with dimension of $\Phi 15.3mm$ was presented to obtain large recovery force, where one SMA wire with diameter of 5.3mm was surrounded by six SMA wires with diameter of 5.0 mm to obtain good clamping capability.

3.2.2. Smart concrete beam manufacture

The smart concrete beam with dimensions 1996cm×99cm×85cm was manufactured, and the cross section is shown in Fig. 29. Sixteen bounds of pre-stressed high-strength steel strands were mounted on the bottom of the beam to resist the normal loads; six bounds of SMA bundle-steel strand union body, numbered 1 to 6 from left to right, respectively, were constructed upside the steel strands to create recovery forces.

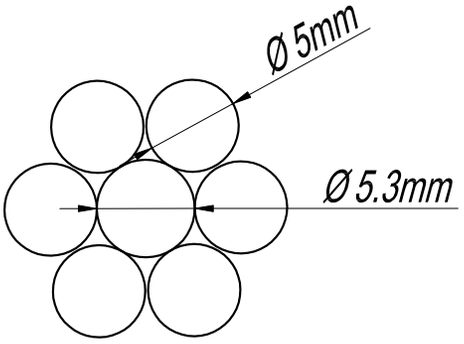

Figure 28. Diagram of SMA bundle

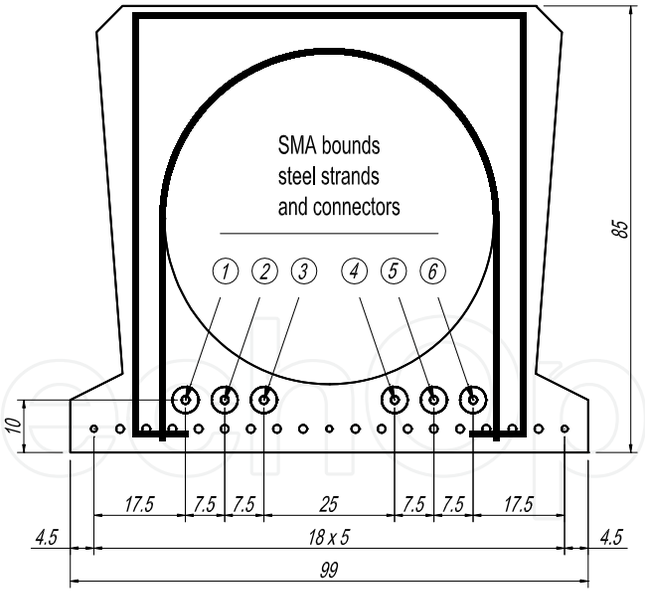

Figure 29. Distribution of cross-section of the smart concrete beam

A new SMA embedding method in concrete was presented, which can be seen in Fig. 30. The SMA bundle measuring 3.5 m long was mounted in the middle of the beam to create recovery forces, and connector was used to connect the SMA bundle with the steel strands. The recovery forces generated by the SMA bundles were transferred to the concrete matrix by the steel strands on the bonding zone measuring 3 m at both ends of the beam. When the

SMA bundles were activated by electricity, additional bending force was generated and applied to the beam, In the unbonded zone, SMA bundles and steel strands were separated from concrete by PVC pipes, therefore the SMA bundles and the connectors could shift freely, and the temperature influence of SMA bundles to the matrix could be decreased as small as possible.

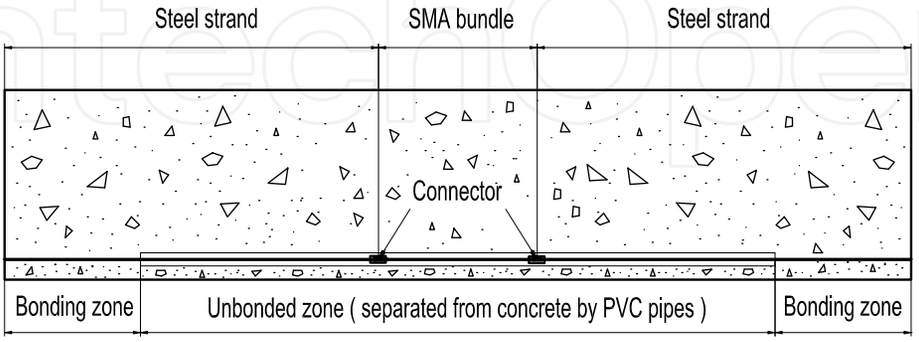

Figure 30. Distribution of longitudinal-section of the smart concrete beam

Sensing and power system of these smart beams can be seen in Fig. 31. Temperature sensors and reinforcement meters were mounted on the SMA bundle, six trusses of SMA bundles were connected in series by voltaic wires to receive the electric power, and copper wiring terminals were used to connect the conductor wires with the SMA bundles. All the sensor wires were laid along the beam at a lower level position and led out at the end of the beam. Two voltaic wires were laid along the beam at a higher level position and led out at the same end of the beam. Considering the effect of steel reinforcement cage, the electric circuit must be constructed as a self-consistent system to avoid short circuit, and all sensor wires and electric cable should be protected from the damage of the construction machinery.

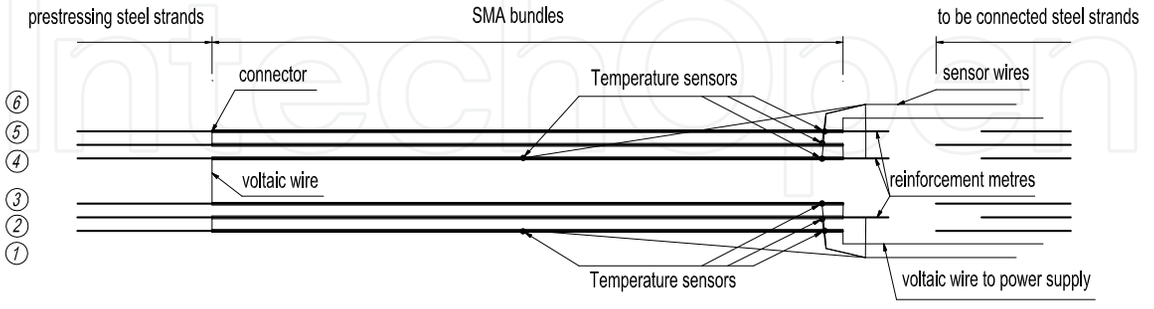

Figure 31. Layout of the sensors and wires

Initial tension of the SMA bundles was carried out after the initial elongation of the steel strands, and the initial strain of the SMA bundles reached 4%. After finishing the stretching of the SMA bundles and steel strands (Fig. 32), concrete was deposited into the steel model and steam was used during the curing period of the concrete.

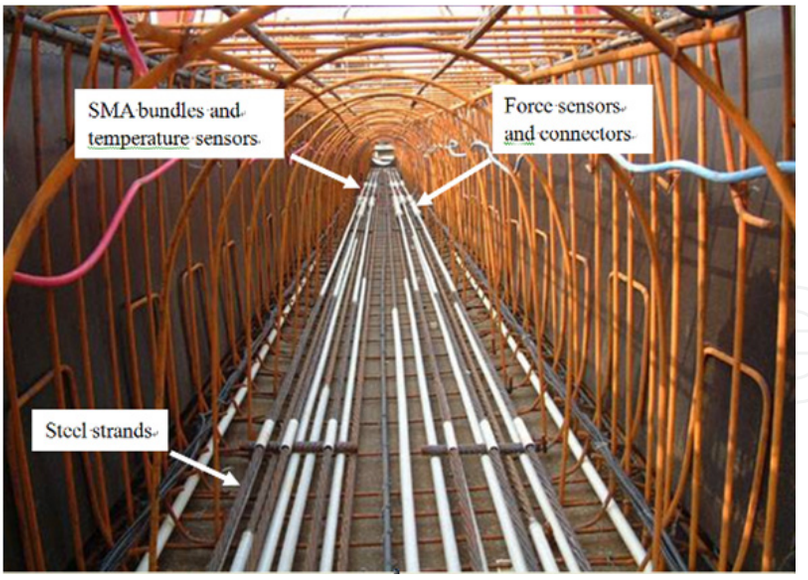

Figure 32. Framework of steel reinforcement with stretched SMA bundles

After about three days, when the concrete strength reached 80 percent of its 28–day strength, SMA bundles and steel strands were relaxed and the concrete beams were lifted out from the model, and tests of these beams were carried out subsequently.

3.2.3. Testing apparatus and procedure

The beam to be monitored was laid on an experimental bench for freely-supported condition, and the testing site is shown in Fig. 33. When the SMA bundles were activated, additional bending forces were generated, and the beam was inflected at the same time. Contrarily, when the SMA bundles were inactivated, the recovery forces disappeared and the beam recurred to the original state, as shown in Fig. 34.

Figure 33. Experiment site

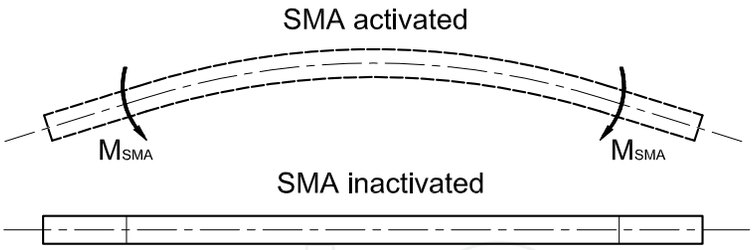

Figure 34. Behavior of the beam with SMA activated and inactivated

The SMA bundles were heated with electricity. Because of the low electrical resistance of the SMA bundles, the necessary voltage was low, but the required current capacity was large, therefore, a 12.5V, 125A variable capacity voltage source was employed to each beam. Experimental results indicated that the resistance of the SMA bundles in each beam was about 0.166 Ω .

Three displacement sensors were mounted at three quartiles of the beam. Deflection of the beam, the temperatures of the SMA bundle, and the recovery forces generated by the SMA bundles, were monitored synchronously during the progress of the experiment. All the data were acquired and analyzed preliminarily through a 16-channel dynamic data-acquisition system. The sampling frequency was 10 Hz, and the maximum sampling frequency could reach 10000Hz.

3.3. Results and discussions

Two beams were manufactured and each was examined for several times. For convenience, beams, SMA bundles and temperature sensors were all numbered by the following principle:

1. Two beams were numbered 1 to 2.
2. Serial number of the SMA bundles of each beam was composed of the number of the beam and relative position label in the same beam, i.e. 2-4. The first number indicated that the SMA bundles belonged to the No. 2 beam and the second number indicated that this is the No. 4 SMA bundle, as depicted in Fig. 29.
3. Temperature sensors were marked by the number of the SMA bundle and the position label, i.e. 1-3-T1. The first number of the temperature sensor label indicates the number of the beam, and the second denotes the number of the SMA bundle where the temperature sensors are mounted on. The symbol T1 denotes that the temperature sensors are mounted in the middle of the SMA bundles, and T2 denotes that the temperature sensors are mounted at the end of the SMA bundles. Thus the flag 1-3-T1 indicates the temperature sensor mounted in the middle of 1-3 SMA bundle.

3.3.1. Deflection of the smart concrete beam

The recovery forces generated by the SMA bundles would induce a bending force on the beam, and cause a deformation of the beam, as depicted in Fig. 34. The deformation of the

beam was indicated by the displacement of the three quartiles on the beam. The effect of the environmental temperature, which was discussed in the following content, was eliminated during this analytic process. Each beam was activated and monitored for several times, and the results were almost similar. The representative results of beam 1 and beam 2 were shown in Fig. 35.

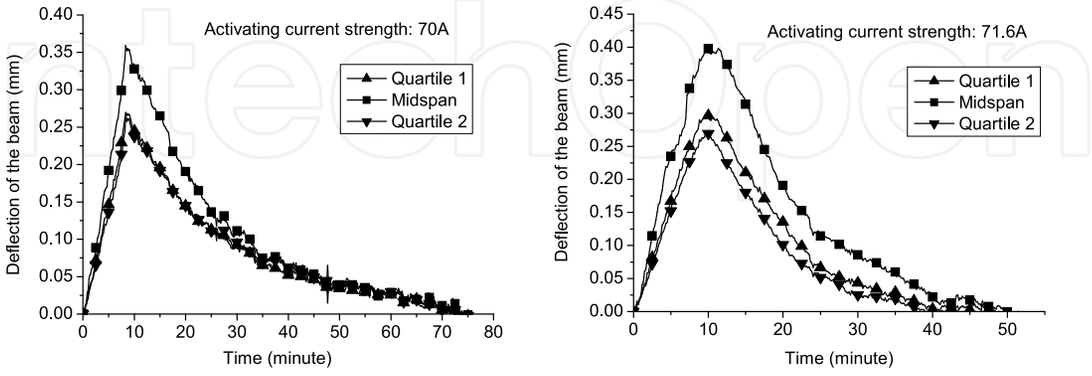

(a). Beam 1 in No.3 activating times (b). Beam 2 in No.9 activating times

Figure 35. Deflection of the beam versus time

3.3.2. Temperature of SMA bundles

When the beam was activated with voltage, temperature of the SMA bundles would rise, and when the current source was shut down, the temperature would drop. The maximum temperature rising speed was at the initial point, as time went on, it decreased and approached to zero, then the thermo-genesis was equal to the heat dissipation and temperature kept up a constant maximum value. Different temperature sensors mounted on the different SMA bundles in a beam detected different temperatures, as shown in Fig. 36. This phenomenon came from the different heat conducting boundary condition of the different SMA bundles. But the results of the same temperature sensor under different activating times were little different, as depicted in Fig. 37, only the temperature dropping section had a little difference yielding from different temperature environment in different activating times.

3.3.3. Recovery force generated by SMA bundles with temperature

When the SMA bundles were activated by voltage, the temperature of these bundles raised and the recovery forces generated and increased, but when the current was cut off, the temperature dropped and the forces decreased. The different force generated by different SMA bundles, this difference yield from the different initial force of the SMA bundles. Force variation with time of some bundles was shown in Fig. 38, and each symbol indicated 1.5 minutes. The recovery forces almost increased proportionally with the rising of the temperature, just as depicted in Fig. 39. Hysteresis cycles were observed in the curve of force versus temperature of SMA bundle 2-4, this phenomenon will be investigated later.

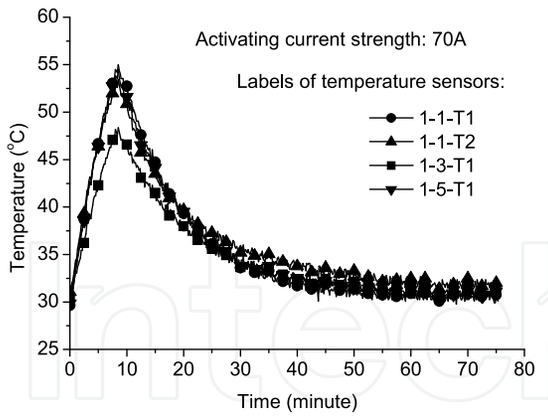

(a). Temperature sensors of beam 1 in No.3 activating times

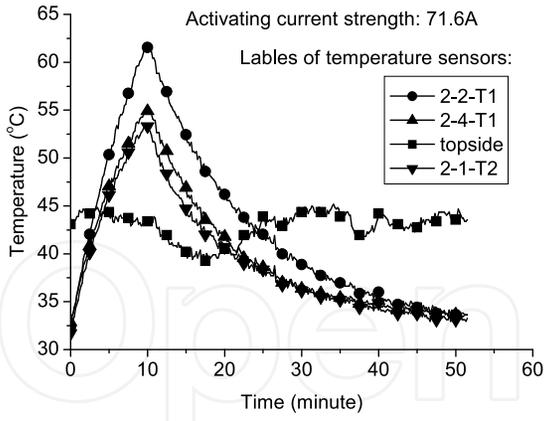

(b). Temperature sensors of beam 2 in No.9 activating times

Figure 36. Temperature versus time for different temperature sensors in the same beam

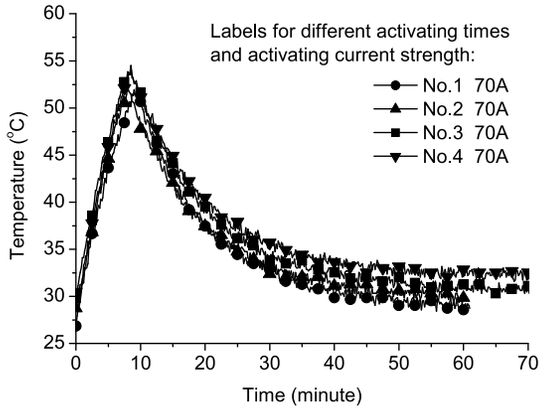

(a). Temperature sensor 1-5-T1

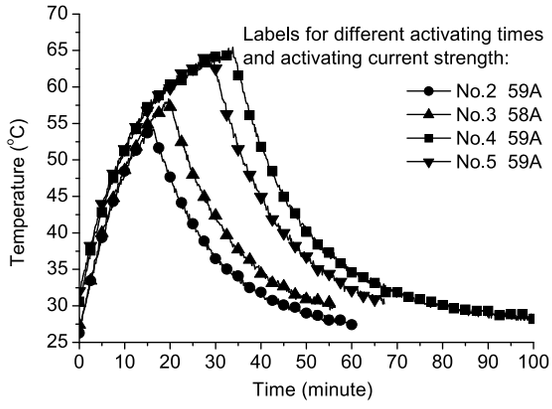

(b). Temperature sensor 2-2-T1

Figure 37. Temperature versus time for different activating times of the same temperature sensor

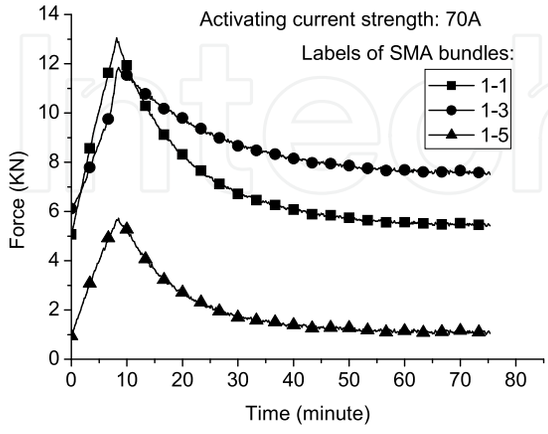

(a). SMA bundles of beam 1 in No.3 activating times

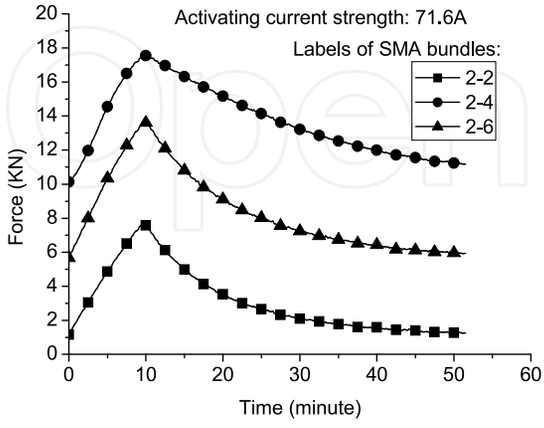

(b). SMA bundles of beam 2 in No. 9 activating times

Figure 38. Force versus time for different SMA bundles of the same beam

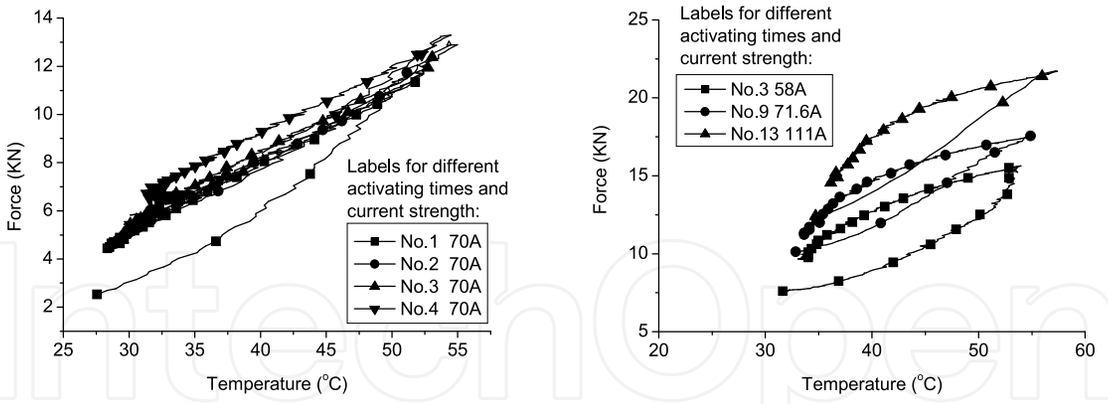

(a). SMA bundle 1-1 (b). SMA bundle 2-4

Figure 39. Force versus temperature for different activating times of the same SMA bundles

3.3.4. Effect of activating current

Effect of the activating current was investigated, current with the strength of 58A, 70A and 110A were applied to the SMA bundles, higher current would induce a faster rising of the temperature of the SMA bundles, thus, the recovery forces increased faster, and the beam reacted with a higher speed, but the recover processes were almost similar, just as depicted in Fig. 40, 41 and 42.

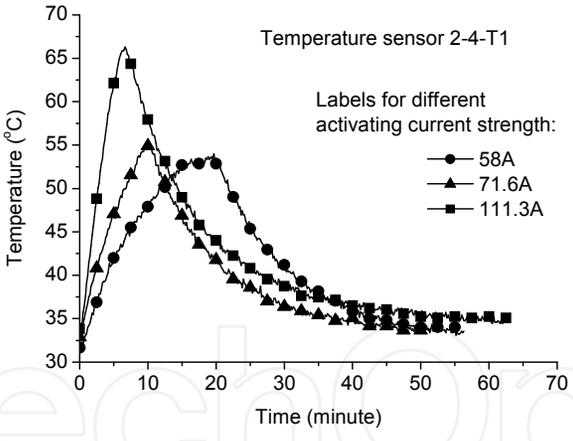

Figure 40. Temperature versus time of temperature sensor 2-4-T1 for different activating current

3.3.5. Effect of environment temperature

During the experiment, the upside temperature of the beam would increase because of the sunshine, while that of the lower side varied rarely. Therefore, this uneven temperature distribution would induce the deflection of the beam. Deformation and the variation of the temperature of the beam also monitored to explain this effect on the deflection of the beam, and the result of this effect was depicted in Fig. 43. Monitoring of No.1 beam was carried out at 9:00 AM and finished at 8:00 PM. The maximum temperature on the upside of the beam (T0) occurred at 3:00 PM, but the maximum deflection the beam at 5:40 PM, this time lag

showed that it needed heat conductivity from the surface to the inner. Temperature on the lower side of the beam varied rarely. In the morning, right-hand of the beam faced the sunshine, and in the afternoon, the left-hand of the beam, therefore, temperature at the right-hand of the beam (T2 and T3) increased faster than that of the left-hand of the beam (T1) in the forenoon, and slower in the afternoon, just as depicted in Fig. 43. During this monitoring course, all the SMA bundles were inactivated, thus the temperatures of the SMA bundles were equal to these of the concrete matrix. From this result, it can be seen that the effect of the environment temperature is considerable.

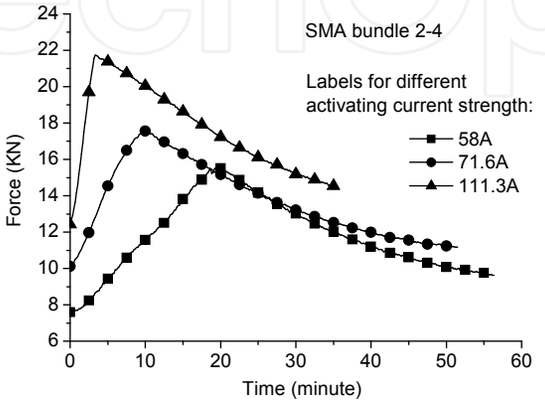

Figure 41. Force versus time of SMA bundle 2-4 of different activating current

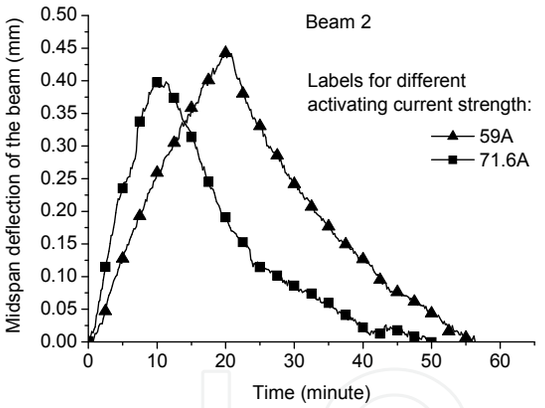

Figure 42. Middle span deflection versus time of beam 2 for different activating current

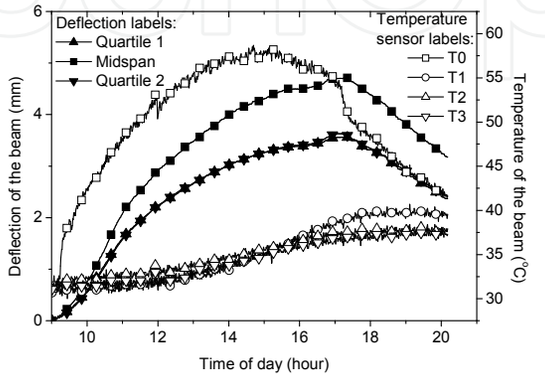

Figure 43. Fig. 43 Effect of environment temperature on deflection and temperature of the beam

3.4. Theoretical analysis

3.4.1. Resisting overload capability

Assuming that a short-term concentrated overload P was applied to the beam, as depicted in Fig. 44, then the overload inducing 1 mm displacement at the middle span of the beam could be calculated.

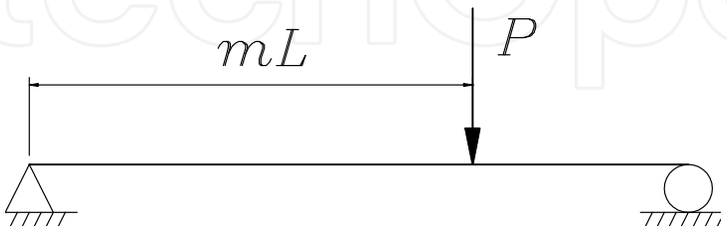

Figure 44. Schematic of load application model

When the overload was applied to the middle span of the beam, the maximum flexural torque at the middle span of the beam generated by the overload was:

$$M_{\max} = \frac{PL}{4} \tag{19}$$

Where P is the overload, and L is the span of the beam.

Thus, the deflection at the middle span of the beam could be given as:

$$f_{\max} = \frac{1}{12}\frac{M_{\max}L^2}{B_{s1}} \tag{20}$$

Where $f_{\max}$ is the maximum deflection of the beam (at the middle span); L is the span of the beam measuring 1996cm; B_{s1} is the flexural rigidity of the beam for short-term load; $M_{\max}$ is the maximum flexural torque at the middle span of the beam.

Thus, the maximum concentrated overload inducing 1 mm displacement at the middle span of the beam could be calculated as:

$$P = \frac{48 f_{\max} B_{s1}}{L^3} = 6.73 \quad \text{KN} \tag{21}$$

Assuming that value of the overload inducing a deflection of 1 mm at the middle span of the beam is equal to that of the resisting force in the negative direction at the middle span of the beam, thus the statistic result of the deflections at the middle span of the beam and the resisting force generated by the SMA bundles for each beam could be seen in table 2.

Beam serial number	The maximum deflection at the middle span of the beam (unit: mm)	Equivalent resisting force (unit: KN)	Activating current strength (unit: A)	Activating time (unit: minute)
No. 1	0.402	2.7055	70	9.3
No. 2	0.482	3.2439	71	16.3

Table 2. Statistic result of deflections at the middle span of the beam and equivalent resisting force of the beams

3.4.2. Curve fitting of experimental results

Considering a section of SMA bundle, if T is defined as the temperature of the SMA bundle, then the increase of T is given as

$$\rho c V_{\mathrm{SMA}} \frac{dT}{d\tau} = q_v V_{\mathrm{SMA}} - a\mu F_{\mathrm{SMA}} \left(T - t_f \right) \tag{22}$$

Where ρ, c, τ and V_{SMA} denote density, specific heat, time and capacity of the SMA bundle; q_v is the rate of heat production; a, μ, F_{SMA} and t_f denote the coefficient of heat convection, quotient of contact face form, area of the heat-exchange surface and ambient temperature.

The rate of heat production $q_v V_{\mathrm{SMA}}$ can also be expressed as follows:

$$q_v V_{\mathrm{SMA}} = I^2 R_{\mathrm{SMA}} \tag{23}$$

Where I and R_{SMA} denote the current strength and electric resistance of SMA.

Thus, equation (4) could be written as:

$$\frac{dT}{d\tau} + \frac{a\mu F_{\mathrm{SMA}}}{\rho c V_{\mathrm{SMA}}} t = \frac{I^2 R_{\mathrm{SMA}}}{\rho c V_{\mathrm{SMA}}} + \frac{a\mu F_{\mathrm{SMA}}}{\rho c V_{\mathrm{SMA}}} t_f \tag{24}$$

Defining

$$X = \frac{I^2 R_{\mathrm{SMA}}}{\rho c V_{\mathrm{SMA}}} \tag{25}$$

$$Y = \frac{a\mu F_{\mathrm{SMA}}}{\rho c V_{\mathrm{SMA}}} \tag{26}$$

Then the solution to equation (24) could be given as:

$$T(\tau) = Ae^{-Y\tau} + \frac{X}{Y} + t_f \tag{27}$$

Where A is related to the initial condition during temperature rising period.

In the same manner, the decrease of T could be given as:

$$\frac{dT}{d\tau}+\frac{a\mu F_{\mathrm{SMA}}}{\rho c V_{\mathrm{SMA}}}T=\frac{a\mu F_{\mathrm{SMA}}}{\rho c V_{\mathrm{SMA}}}t_f \tag{28}$$

Thus from equations (26) and (28), we have:

$$T(\tau)=Be^{-Y\tau}+t_f \qquad (\text{When } I=0) \tag{29}$$

Where B is related to the initial condition during temperature dropping period.

The experimental curve could be fitted well with this theoretical curve, just as depicted in Fig. 45.

Considering equation (22), temperature rising rate of the SMA bundles $dT/d\tau$ could be given as:

$$\frac{dT}{d\tau}=\frac{I^2R_{\mathrm{SMA}}}{\rho c V_{\mathrm{SMA}}}+\frac{a\mu F_{\mathrm{SMA}}}{\rho c V_{\mathrm{SMA}}}(t_f-T) \tag{30}$$

Assuming that the temperature T was equal to the environment temperature t_f at the beginning, then the initial temperature rate of the SMA bundles $dT/d\tau$ can be given as

$$\frac{dT}{d\tau}=\frac{R_{\mathrm{SMA}}}{\rho c V_{\mathrm{SMA}}}I^2 \tag{31}$$

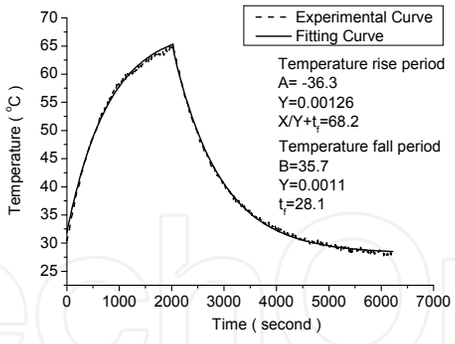

Figure 45. Fitting curve of temperature versus time of temperature sensor 2-2-T1 in NO.4 activating times

According to the above theory, statistic values of the initial temperature rising rate were fitted with the numerical curve, just as depicted in Fig. 46. From it, one can see that the activating current strength had significant effects on the behavior of the smart beam, and higher activating current could be used to achieve a faster reacting speed of the beam. According to the above analyses, the action speed was the proportion square of the current strength.

Theoretically, the temperature of SMA is proportional to the square of the applied current because of this electric heating method. As a matter of fact, this relationship may be affected

by many factors, e.g. the heat transfer from the SMA to the concrete matrix. Here, the well accord between the experimental data and the fitting curve indicated that influences of heat transfer between the SMA and the concrete matrix could be decreased effectively by separating SMA bundles from concrete matrix by PVC pipes.

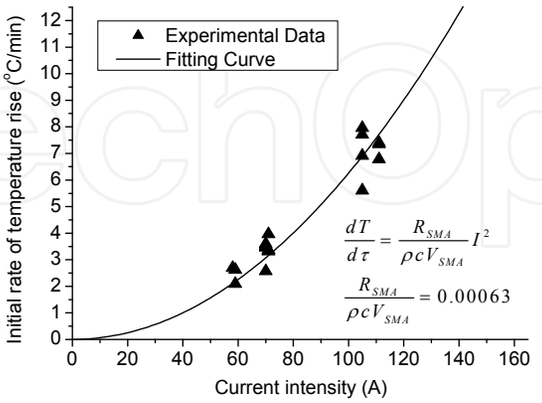

Figure 46. Fitting curve of temperature rising rate versus current intensity

3.5. Conclusions

In this section, the manufacture process and behavior of the smart concrete beams with embedded SMA bundles were investigated through an extensive experimental program. The main parameters, such as temperature and recovery force of SMA bundles and the deflection of the concrete beam, were monitored through this program. Major factors influencing the behavior of the beams were examined. From these results, the following conclusions can be drawn.

1. SMA can be used in practical civil engineering structures to resist overload, the effect is considerable. SMA bundles can change the mechanical performance of the smart concrete beam as needed. In this section, a new SMA embedding method in concrete was presented and applied to this experiment -- only a short section of SMA bundle could generate large force, which was mainly due to the large recoverable deformation of SMA.
2. The recovery force created by the SMA bundles was almost proportional to the temperature of the SMA bundles, and hysteresis cycles were observed in the recovery force-temperature curve of some SMA bundles. The recovery force generated by each SMA bundle was different, which came from the different initial condition for different bundles. But the increments of the recovery force of each SMA bundle in each activating time were almost the same.
3. The temperature of different SMA bundles was different, and temperature of a same SMA bundle in different activating times was also little different. These differences yielded from the different heat conducting condition of different SMA bundles and the different environment boundary condition in different activating times. Due to these differences, more force sensors and temperature sensors would be obligatory for more comprehensive monitoring of the beam.

4. The effect of the environment was remarkable, and displacement at the middle span of the beam induced by the environment temperature was about twelve as times as that caused by the recovery force of SMA bundles. Thus, this effect must be considered during the experimental and analytic process.

Some other factors, such as the activating times, the length of the unbonded section, the length of the SMA bundles, the pre-strain of the SMA bundles, and the curing condition of the concrete, etc., can also affect the behavior of the concrete beam. These effects deserve more investigation.

4. Behavior of a smart concrete bridge with embedded SMA bundles

Since there are many differences between the laboratory researches and the practical applications of using this smart material to structural active controlling; thus, it would be worthful and necessary to study how to apply SMA on a practical concrete bridge and how to use the "smart" forces. Accordingly, the objective of this section is to investigate the behavior of a smart concrete bridge with embedded SMA bundles.

The bridge was a simply-supported pre-stressed concrete one with 20 meters long and 12.5 meters wide, and composed of ten ordinary concrete beams and two smart concrete ones measuring 1996cm×99cm×85cm. When the SMA bundles were activated, additional bending forces were generated, and the beam was inflected to resist excessive load at the same time. Otherwise when the SMA bundles were inactivated, the smart forces disappeared and the beam recovered to the initial state. In order to monitor the active control effect of the SMA bundles, some temperature sensors, reinforcement meters and displacement sensors were employed. All the data were acquired through a 16-channel dynamic data-acquisition system. The bridge was examined several times with different activating current intensity, and some static load tests were also carried out to evaluate the capability of resisting overload of the bridge. The experimental results indicate that the smart forces induced by SMA bundles were significant and controllable, the deflection generated by the SMA bundles at the middle span of the bridge was about 0.03 mm, and the capability of resisting excessive load of the smart beams was 5.6 ~ 7.5 KN. It is also shown that SMA could be used as active controlling actuator in civil engineering structures.

4.1. Experimental program

4.1.1. Design concept of the smart concrete bridge

A complete smart concrete bridge in a freeway should contain the following three parts: load and speed sensors mounted at several miles beyond the bridge; control unit and power supply; actuators, temperature and force sensors, and the bridge matrix, the design concept of the smart bridge was demonstrated in Fig. 47.

The two smart beams will be fixed on the smart bridge. In the session of the freeway, load and speed sensors will be amounted at several miles away from the bridge. Therefore, SMA

bundles embedded in the smart beams can be activated before the load exerts on it and recovery forces generate to resist the external load. Additionally, the recovery force generated by the SMA bundles is only used to resist the excessive load when needed, normal load is resisted by ordinary structures, such as steel reinforcements and steel strands. After the load passes the bridge, SMA bundles will be inactivated.

4.1.2. Manufacturing the beams and the bridge

The bridge was composed of twelve concrete beams, and the two smart concrete beams were fixed on the No. 5 and No. 6 from outer side (Fig. 48). Gaps between the beams were filled up with concrete, and then the surface concrete and the pavement were constructed subsequently.

4.1.3. Testing apparatus and procedure

The two smart concrete beams were electrically activated several times to measure the effect of the recovery forces. To evaluate the performance of the bridge, the static load tests were also carried out by parking a 202KN-weight truck on the nine positions of the bridge (Fig. 49).

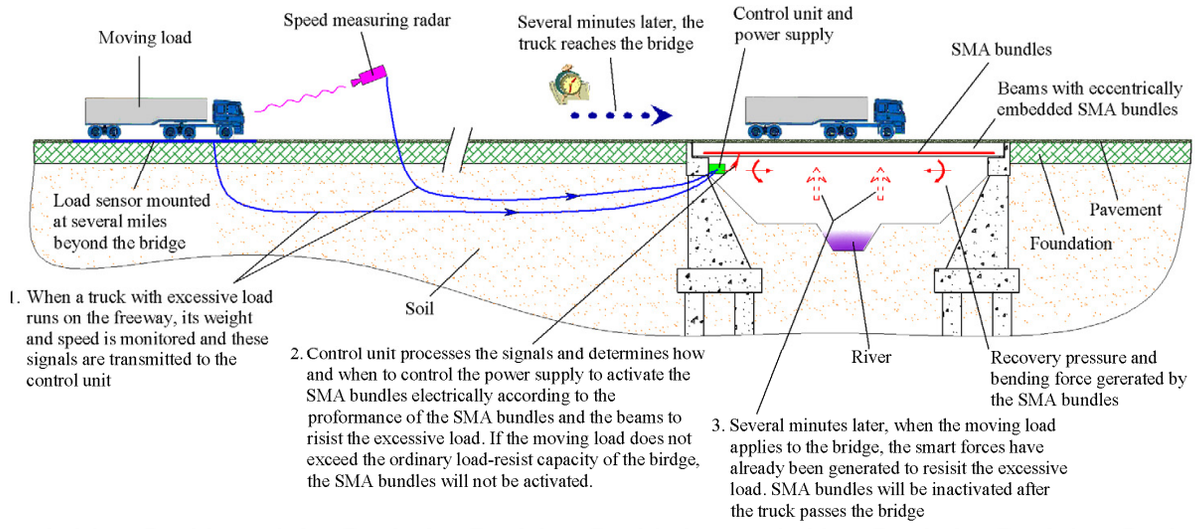

Figure 47. Diagram of the design concept about a smart bridge of a freeway

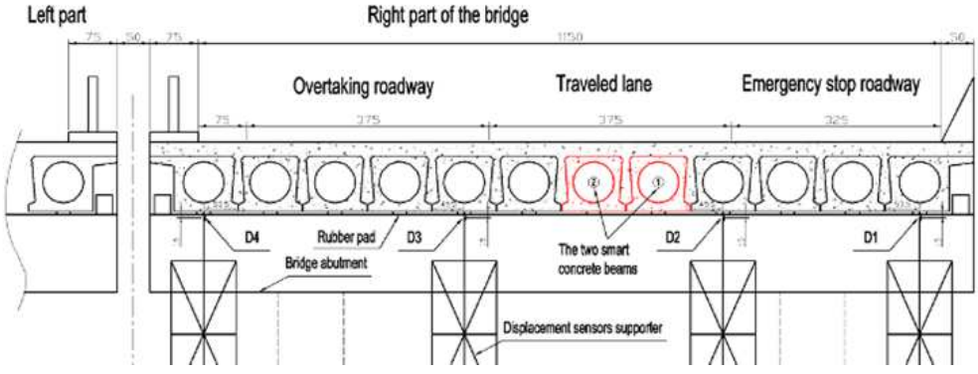

Figure 48. Schematic of mounting deflection sensors

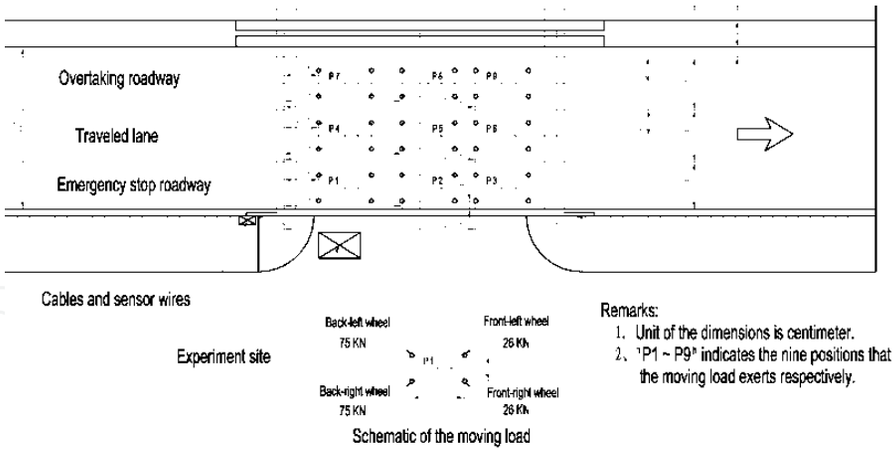

Figure 49. Schematic of static load test

4.2. Results and discussions

In order to record easily, the SMA bundles, temperature and force sensors were numbered serially. Two beams were numbered 1 and 2, and SMA bundles, 1 to 6. Thus SMA bundles and the force sensors can be indicated with the number of the beam and the relative position label in the same beam. The temperature sensor was denoted via the number of the SMA bundle and its position label (i.e. T1 denotes the temperatures mounted at the middle of the SMA bundle, T2 the end).

4.2.1. Activating test results of the bridge

To evaluate the effect of the recovery force, the SMA bundles of the two smart concrete beams were activated two times without applying any external load on the bridge. Displacement sensors were mounted at the bottom of No 1, 4, 8, 12 beams of the bridge (denoted by D1, D2, D3, D4 respectively) to monitor its deformation, as shown in Fig. 48.The unit of the dimensions is centimeter, and D1, D2, D3, D4 indicates the four positions that the displacement sensors mounted on respectively. Temperatures, as well as recovery forces, were also measured synchronously during the experiment.

When the SMA bundles were activated, the bridge was deformed and upward deflections were induced. Deflections at the middle span of the bridge increased and decreased during the activating and inactivating, as shown in Fig. 50. The maximum deflection of the bridge was about 0.03mm. Displacement sensor mounted at the D1 position did not work normally, so the result will be not considered in the analysis.

During the heating and cooling process, temperatures of SMA bundles also increased and decreased, as shown in Fig. 51, and recovery forces of SMA bundles increased and decreased proportionally with these temperatures, as shown in Fig. 52. The recovery force created by the SMA bundles was almost proportional to the temperature of the SMA bundles, and hysteretic cycles were observed in the recovery force-temperature curve of the SMA bundles.

4.2.2. Static test results of the bridge

The static load was applied on the nine positions of the bridge, as shown in Fig. 49, deflections at the four representative points of the bridge (indicated as D1, D2, D3, D4) were demonstrated in Fig. 53.

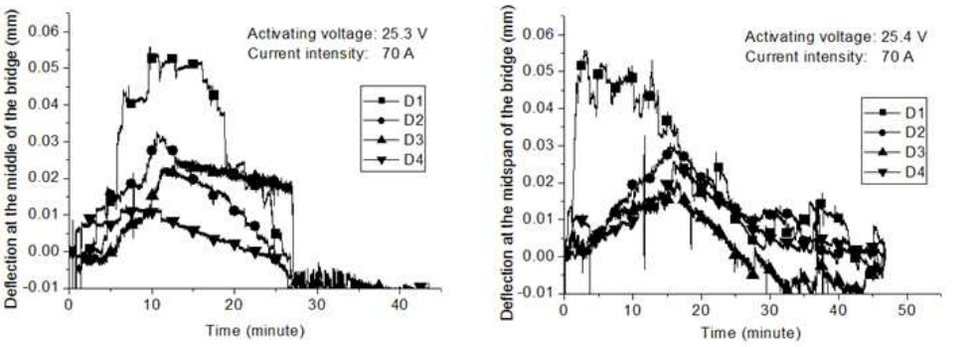

Figure 50. Deflection at the middle of the bridge versus time

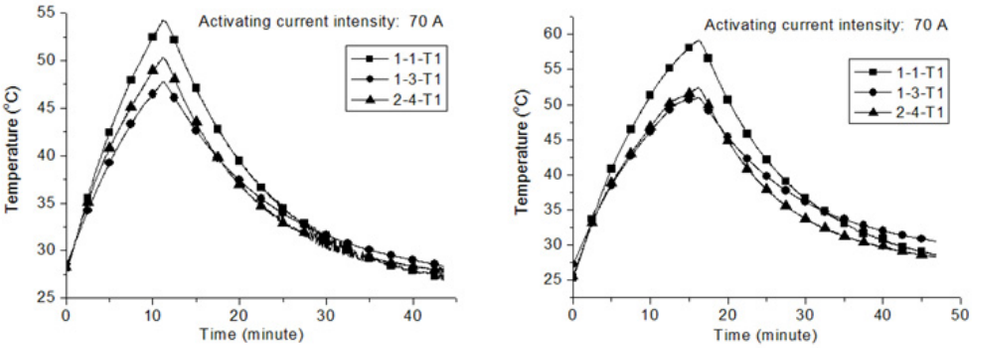

Figure 51. Temperature of SMA bundles versus time

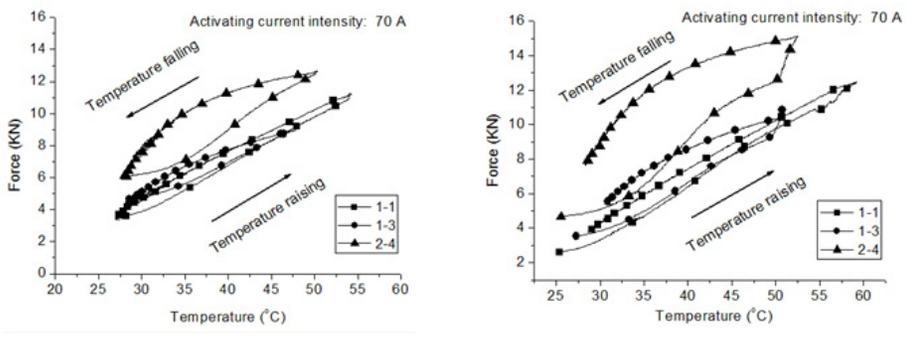

Figure 52. Recovery force versus temperature

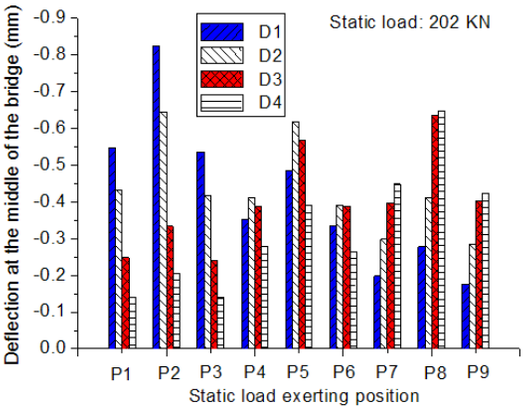

Figure 53. Deflection of the bridge under different load exerting positions

4.2.3. Effect analysis of the recovery forces

The capability of resisting excessive load of recovery forces was estimated through the following principle: all the deflections at the D1, D2, D3, D4 induced by the recovery forces are larger than or equal to these reverse ones induced by the external load. Therefore, by comparing the average maximum deflections of the activating test and deflections of the static load test, the maximum resisting load capability could be obtained. Different position the excessive load exerted on is, different the resisting load of the SMA bundles.

When the load ran on the middle of the traveled lane, deflection of the beam No.8 induced by the recovery forces reached the reverse one by the external load firstly, thus the resisting load of the recovery forces was about 7.53 KN shown in Fig. 54 (a), and on the overtaking roadway, 5.55 KN in Fig. 54 (b).

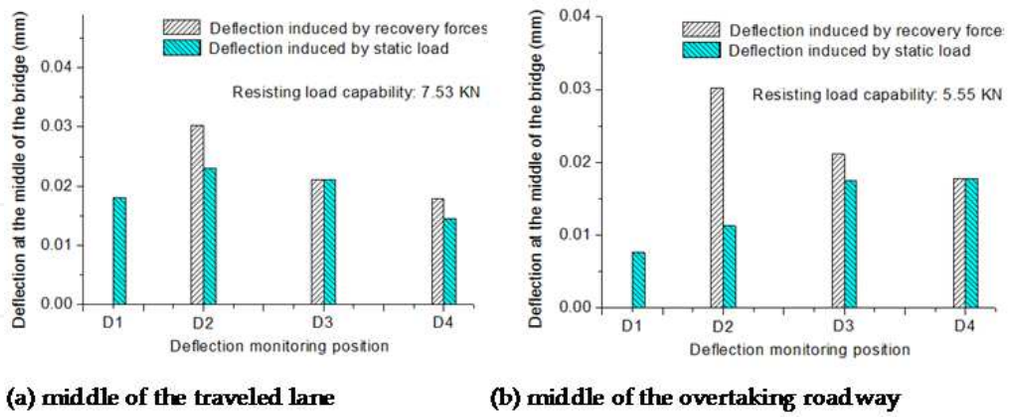

Figure 54. Resisting load analysis

4.3. Conclusions

In this section, the manufacturing process and the behavior of the smart concrete bridge with embedded SMA bundles were investigated. From these results, the following conclusions can be drawn: (1) SMA can be used in practical concrete bridges to resist

external load with considerable effect. SMA bundles can change the mechanical performance of the smart concrete beam as needed; (2) The capability of resisting excessive load of the recovery forces can be varied with the different exerting position of the external load, thus the optimum design of the smart concrete structures will be necessary to obtain the best control effect.

5. Remarks

In this chapter, the constitutive characteristics of NiTi SMA and its application in practical concrete structures were investigated. The experimental results indicated that the mechanical properties and the phase transformation characters of NiTi SMA could be affected by the loading process considerably. Comparison between the numerical and experimental results indicated that the proposed model could simulate the phase transformation characters, the uniaxial tension and the constrained recovery behavior of NiTi SMA more effectively. Experimental results indicated that the additional recovery forces generated by the SMA could be changed by altering its temperature, and can be used to adjust the deflection of the concrete bridge and to enhance the load-bearing capability of the concrete bridge.

Author details

Lei Li
State Key Laboratory of Hydroscience and Engineering, Tsinghua Univ., Beijing, P. R. China
China Three Gorges Corporation, Beijing, P. R. China

Qingbin Li*
State Key Laboratory of Hydroscience and Engineering, Tsinghua Univ., Beijing, P. R. China

Fan Zhang
Dept. of Transportation of Henan Province, Zhengzhou, P. R. China

6. References

Anders, W. S., Rogers, C. A., & Fuller, C.R. 1990. "Vibration and low frequency acoustic analysis of piecewise-activated adaptive composite panels," *Journal of Composite Materials*, Vol.26, No.1, pp.103-120.

Baz, A., Imam, K., & Mccoy, J. 1990. "Active vibration control of flexible beams using shape memory actuators," *Journal of Sound and Vibration*, Vol.140, No.3, pp.437-456.

Baz, A., Poh, S., & Gilheany, J. 1995. "Control of the natural frequencies of Nitinol-reinforced composite beams," *Journal of Sound and Vibration*, Vol.185, No.1, pp.171-183.

Baz, A., & Tampa, L. 1989. "Active control of buckling of flexible beams," *Failure Prevention & Reliability*, ASME, pp.211-218.

* Corresponding Author

Brinson, L. C. 1993. "One-dimensional constitutive behavior of shape memory alloys: thermomechanical derivation with non-constant material functions and redefined martensite internal variable," *Journal of Intelligent Material Systems and Structures*, Vol.4, No.2, pp.229-242.

Brocca, M., Brinson, L. C., & Bazant, Z. P. 2002. "Three-dimensional constitutive model for shape memory alloys based on microplane model," *Journal of the Mechanics and Physics of Solids*, Vol.50, No.5, pp.1051-1077.

Buehler, W. J., Gilfrich, J. V., & Wiley, R. C. 1963. "Effect of low-temperature phase changes on the mechanical properties of alloys near composition TiNi," *J. Appl. Phys.*, Vol.34, No.5, pp.1475-1477.

Chaudhry, Z., & Rogers, C. A. 1991. "Bending and shape control of beams using SMA actuators," *J. Intelligent Mat. Syst. Struct.*, Vol.2, No.4, pp.581-602.

Choi Sup, Lee Jung Ju, Seo Dae Cheol, & Choi Sun Woo. 1999. "The active buckling control of laminated composites beams with embedded shape memory alloy wires," *Composite Structures*, Vol.47, No.1-4, pp.679-686.

Choi Sup, Lee Jung Ju, Seo Dae Cheol, & Dong Kusong. 2000. "A study on the bucking and postbuckling control of composite beams with embedded NiTi actuators," *Journal of Composite Materials*, Vol.34, No.17, pp.1494-1510.

Crawley Edward F. 1994. "Intelligent structures for aerospace: a technology overview and assessment," *AIAA Journal*, Vol.32, No.8, pp.1689-1699.

Deng Zongcai, Li Qingbin, Jiu Anquan, & Li Lei. 2003. "Behavior of Concrete Driven by Uniaxially Embedded Shape Memory Alloy Actuators," *Journal of Engineering Mechanics*, Vol.129, No.6, pp.697-703.

Delaey, L., Krishnan, R. V., Tas, H., & Warlimont, H. 1974. "Thermoelasticity, pesudoelasticity and the memory effects associated with martensitic transformations (part 1 structural and microstructrual changes associated with the transformations)," *Journal of Materials Science*, Vol.9, No.9, pp.1521-1535.

Funakubo Hiroyasu. (Translated from Japanese by Kennedy J.B.) 1987. "Shape Memory Alloys," *Gordon and Breach Science Publishers*, New York.

Greninger, A.B., & Mooradian, V.G. 1938. "Strain transformation in metastable beta copper-zinc and beta copper-tin alloys," *Trans. Met. Soc. AIME*, Vol.128, pp.337-368.

Graesser, E. J., & Cozzarelli, F. A. 1991. "Shape-memory alloys as new materials for aseismic isolation," *ASCE Journal of Engineering Mechanics*, Vol.117, No.11, pp.2590-2608.

Greninger, A. B., & Mooradian, V. G. 1938. "Strain transformation in metastable beta copper-zinc and beta copper-tin alloys," *Trans. Met. Soc. AIME*. Vol.128, pp.337-368.

Jonnalagadda, K., Kline, G. E., & Sottos, N. R. 1997. "Local displacements and load transfer in shape memory alloy composites," *Experimental Mechanics*, Vol.37, No.1, pp.78-86.

Krishnan, R. V., Delaey, L., Tas, H., & Warlimont, H. 1974. "Thermoelasticity, pesudoelasticity and the memory effects associated with martensitic transformations (part 2 the macroscopic mechanical behaviour)," *Journal of Materials Science*, Vol.9, No.9, pp.1536-1544.

Liang Chen. 1990. "Constitutive modeling of shape memory alloys," PhD Thesis, VPI, Blacksburg, VA.

Lagoudas Dimitris C., & Tadjbakhsh Iradj G. 1992. "Active flexible rods with embedded SMA fibers," *Smart Mater. Struct.*, Vol.1, No.2, pp.162-167.

Lau Kin-tak, Zhou Limin, & Tao Xiaoming. 2002. "Control of natural frequencies of a clamped-clamped composite beam with embedded shape memory alloy wires," *Composites Structures*, Vol.58, No.1, pp.39-47.

Maji Arup K., & Negret Ihosvany. 1998. "Smart prestressing with shape-memory alloy," *Journal of Engineering Mechanics*, Vol.124, No.10, pp.1121-1128.

Matsuzaki Yuji. 1997. "Smart strutures research in Japan," *Smart Mater. Struct.*, Vol.6, No.4, pp.1-10.

Otsuka, K., & Wayman, C. M. 1998. "Shape Memory Materials," Cambridge University Press, Cambridge, UK; New York, USA.

Song Gangbing, Kelly Brian, & Agrawal Brij N. 2000. "Active position control of a shape memory alloy wire actuated composite beam," *Smart Mater. Struct.*, Vol.9, No.5, pp.711-716.

Srinivasan, A.V., & Mcfarland D. Michael. 2001. "Smart Structures: Analysis and Design," Cambridge University Press, Cambridge, UK; New York, USA.

Sun Qingping, & Hwang Keh Chin. 1993a. "Micromechanics modeling for the constitutive behavior of polycrystalline shape memory alloy – I. Derivation of general relations," *J. Mech. Phys. Solids*, Vol.41, No.1, pp.1-17.

Sun Qingping, & Hwang Keh Chin. 1993b. "Micromechanics modeling for the constitutive behavior of polycrystalline shape memory alloy – II. Study of the individual phenomena," *J. Mech. Phys. Solids*, Vol.41, No.1, pp.19-33.

Tanaka K. 1986. "A thermomechanical sketch of shape memory effect: one-dimensional tensile behavior," *Res Mechanica*, Vol.18, pp.251~263

Tanaka, K., & Nagaki, S. 1982. "A thermomechanical description of material with internal variable in the process of phase transitions," *Ingenieur-Archiv*, Vol.51, No.5, pp.287-299.

Warlimont, H., Delaey, L., Krishnan, R. V., & Tas, H. 1974. "Thermoelasticity, pesudoelasticity and the memory effects associated with martensitic transformations (part 3 thermodynamics and kinetics)," *Journal of Materials Science*, Vol.9, No.9, pp.1545-1555.

Zhu Jiujiang, Liang Naigang, Huang Weimin, & Liu Zhihong. 2002. "A thermodynamic constitutive model for stress induced phase transformation in shape memory alloys," *International Journal of Solids and Structures*, Vol.39, No.3, pp.741-763.